

Backpropagation through space, time and the brain

Benjamin Ellenberger*, Paul Haider*,
Jakob Jordan, Kevin Max, Ismael Jaras, Laura Kriener, Federico Benitez,
Mihai A. Petrovici

*Shared first authorship

Department of Physiology, University of Bern, 3012 Bern, Switzerland.

Abstract

How physical networks of neurons, bound by spatio-temporal locality constraints, can perform efficient credit assignment, remains, to a large extent, an open question. In machine learning, the answer is almost universally given by the error backpropagation algorithm, through both space and time. However, this algorithm is well-known to rely on biologically implausible assumptions, in particular with respect to spatio-temporal (non-)locality. Alternative forward-propagation models such as real-time recurrent learning only partially solve the locality problem, but only at the cost of scaling, due to prohibitive storage requirements.

We introduce Generalized Latent Equilibrium (GLE), a computational framework for fully local spatio-temporal credit assignment in physical, dynamical networks of neurons. We start by defining an energy based on neuron-local mismatches, from which we derive both neuronal dynamics via stationarity and parameter dynamics via gradient descent. The resulting dynamics can be interpreted as a real-time, biologically plausible approximation of backpropagation through space and time in deep cortical networks with continuous-time neuronal dynamics and continuously active, local synaptic plasticity. In particular, GLE exploits the morphology of dendritic trees to enable more complex information storage and processing in single neurons, as well as the ability of biological neurons to phase-shift their output rate with respect to their membrane potential, which is essential in both directions of information propagation. For the forward computation, it enables the mapping of time-continuous inputs to neuronal space, effectively performing a spatio-temporal convolution. For the backward computation, it permits the temporal inversion of feedback signals, which consequently approximate the adjoint variables necessary for useful parameter updates.

1 Introduction

The world in which we have evolved appears to lie in a Goldilocks zone of complexity: it is rich enough to produce organisms that can learn, yet also regular enough to be learnable by these organisms in the first place. Still, regular does not mean simple; the need to continuously interact with and learn from a dynamic environment in real time faces these agents – and their nervous systems – with a challenging task.

One can view the general problem of dynamical learning as

one of *constrained minimization*, i.e., with the goal of minimizing a behavioral cost with respect to the parameters θ that describe these nervous systems, under constraints given by their physical characteristics. For example, in the case of biological neuronal¹ networks, such dynamical constraints may include leaky integrator membranes and nonlinear output filters. The standard approach to this problem in deep learning uses stochastic gradient descent, coupled with some type of automatic differentiation algorithm that calculates gradients via reverse accumulation [1, 2]. These methods are efficient in their use of resources, and flexible in their range of applications.

If the task is time-independent, or can be represented as a time-independent problem, the standard error backpropagation algorithm provides this efficient backward differentiation [3–5]. We refer to this class of problems as *spatial*, as opposed to more complex *spatio-temporal* problems, such as sequence learning. For the latter, the solution to constrained minimization can be sought through a variety of methods. When the dynamics are discrete, the most commonly used method is backpropagation through time (BPTT) [6, 7]. For continuous-time problems, optimization theory provides a family of related methods, the most prominent being the adjoint method (AM) [8], Pontryagin’s maximum principle [9, 10], and the Bellman equation [11].

AM and BPTT have proven to be very powerful methods, but it is not clear how they could be implemented in physical neuronal systems that need to function and learn continuously, in real time, and using only information that is locally available at the constituent components [12]. AM/BPTT cannot be performed online, as it is only at the end of a task that errors are calculated retrospectively (Fig. 1). This requires either storing the entire trajectory of the system (i.e., for all of its dynamical variables) until a certain update time, and/or recomputing the necessary variables during backward error propagation. While straightforward to do in computer simulations (computational and storage inefficiency notwithstanding), a realization in physical neuronal systems would require a lot of additional, complex circuitry for storage, recall and (reverse) replay. Additionally, it is unclear how useful errors can be represented and transmitted in the first place, i.e., which physical network components calculate errors that correctly account for the ongoing dynamics of the system, and

¹We use the term *neuronal* to differentiate between physical, time-continuous dynamical networks of neurons and their abstract, time-discrete artificial neural network (ANN) counterparts.

how these then communicate with the components that need to change during learning (e.g., the synapses in the network). It is for these reasons that AM/BPTT sits firmly within the domain of machine learning, and is largely considered irrelevant for physical neuronal systems, carbon and silicon alike.

Instead, theories of biological (or bio-inspired) spatio-temporal learning focus on other methods, either by using reservoirs and foregoing the learning of deep weights altogether, or by using direct and instantaneous output error feedback, transmitted globally to all neurons in the network, as in the case of FORCE [13] and FOLLOW [14]. Alternatively, errors can also be carried forward in time and associated with past network states, as proposed in real-time recurrent learning (RTRL) [15]. While still suffering from similar spatial locality problems as BPTT, RTRL is temporally causal (Fig. 1). However, this comes at a significant cost in its memory footprint (cubic scaling for RTRL vs. linear scaling for BPTT), which quickly becomes prohibitive for larger-scale applications in machine learning. Various approximations of RTRL alleviate some of these issues [16], but only at the cost of propagation depth. We return to these methods in the discussion, as our main focus here is AM/BPTT.

Indeed, and contrary to prior belief, we suggest that physical neuronal systems can approximate BPTT very efficiently and with excellent functional performance. More specifically, we propose the overarching principle of Generalized Latent Equilibrium (GLE) to derive a comprehensive set of equations for inference and learning that are local in both time and space (Fig. 1). These equations fully describe a dynamical system running in continuous time, without the need for separate phases, and undergoing only local interactions. Moreover, they describe the dynamics and morphology of structured neurons performing both *retrospective* and *prospective* coding, as well as the weight dynamics of error-correcting synapses, thus linking to experimental observations of cortical dynamics and anatomy. Due to its manifest locality and reliance on rather conventional analog components, our framework also suggests a blueprint for powerful and efficient neuromorphic implementation.

We thus propose a new solution for the spatio-temporal credit assignment problem in physical neuronal systems, with significant advantages over previously proposed alternatives. Importantly, our framework does not differentiate between spatial and temporal tasks and can thus be readily used in both domains. As it represents a generalization of Latent Equilibrium (LE) [17], it implicitly contains (spatial) backpropagation as a sub-case.

This manuscript is structured as follows: In Section 2.1, we propose a set of four postulates from which we derive network structure and dynamics. This approach is strongly inspired by approaches in theoretical physics, where a specific energy function provides a unique reference from which everything else follows. The derivation of network dynamics is made explicit in Section 2.2. In Section 2.3 we discuss how these dynamics effectively implement an approximation of AM/BPTT. In Section 2.4 we show how our framework describes physical networks of neurons, with implications for both cortex and

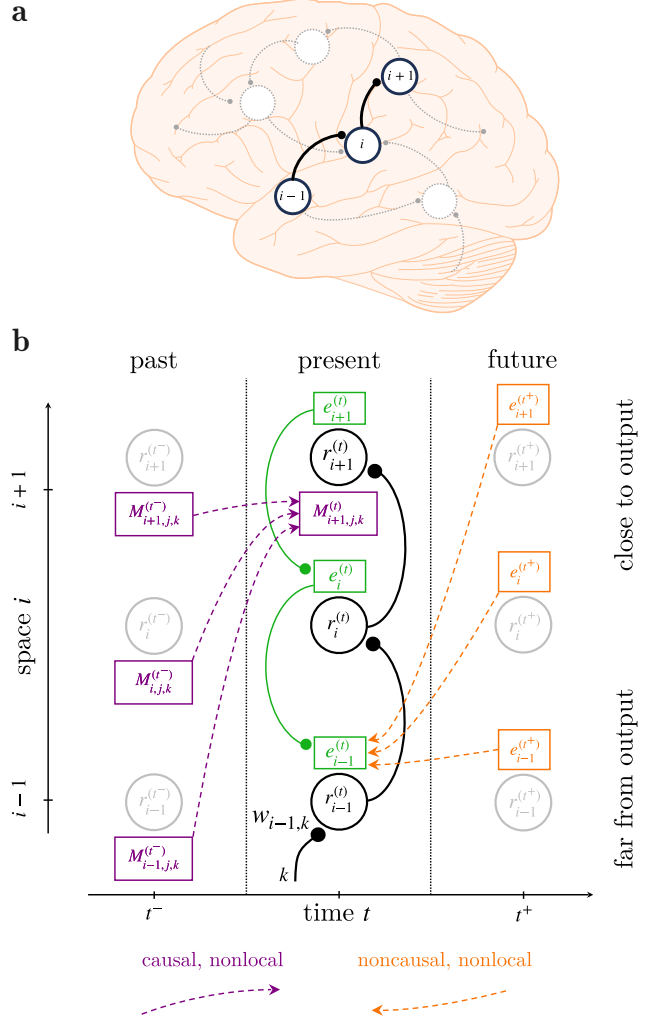


Figure 1: The problem of locality in spatio-temporal credit assignment. (a) To illustrate the different learning algorithms, we consider three neurons within a larger recurrent network. The neuron indices are indicative of the distance from the output, with neuron $i + 1$ being itself an output neuron, and therefore having direct access to an output error e_{i+1} . (b) Information needed by a deep synapse at time t to calculate an update $\dot{w}_{i-1,k}^{(t)}$. These states are used to calculate future errors $e_n^{(t+)}$ for all neurons ($n \leq N$) in the network, which are then backpropagated into present errors $e_n^{(t)}$. Orange: future-facing algorithms such as BPTT need to store the states of all N neurons in the network for all future times t^+ and can therefore only be implemented in an offline fashion. These can then be used for synaptic updates $\dot{w}_{i-1,k}^{(t)} \propto e_{i-1}^{(t)} r_k^{(t)}$. Purple: past-facing algorithms such as RTRL store the effect of all synapses on all past states $r_n^{(t-)}$ in an influence tensor $M_{i,j,k}^{(t-)}$. This tensor can be updated online and used to perform weight updates $\dot{w}_{i-1,k}^{(t)} \propto e_{i+1}^{(t)} M_{i+1,i-1,k}^{(t)}$. Note that all synapse updates need to have access to distant output errors. Furthermore, the update of each element in the influence tensor requires the knowledge of distant elements and is thus itself nonlocal in space. Green: GLE operates exclusively on present states $r_n^{(t)}$. It uses them to infer errors $e_n^{(t)}$ that approximate the future backpropagated errors of BPTT.

hardware. In Section 3, we discuss various applications, from small-scale setups that allow an intuitive understanding of our network dynamics, to larger-scale networks capable of solving difficult spatio-temporal classification problems. Finally, we discuss the connections and advantages of our framework when compared to other approaches in Section 4.

2 Theory

2.1 The GLE framework

At the core of our framework is the realization that biological neurons are capable of performing two fundamental temporal operations. First, as is well-known, neurons perform temporal integration in the form of low-pass filtering. We describe this as a “retrospective” operation, as it is a function of past inputs, and denote it with the operator

$$\mathcal{I}_{\tau^m}^- \{x\}(t) := \frac{1}{\tau^m} \int_{-\infty}^t x(s) \exp\left(-\frac{t-s}{\tau^m}\right) ds, \quad (1)$$

where τ^m represents the membrane time constant and x the synaptic input.

The second temporal operation is much less known but well-established physiologically [18–22]: neurons are capable of performing temporal differentiation, an inverse low-pass filtering that phase-shifts inputs into the future, which we thus name “prospective” and denote with the operator

$$\mathcal{D}_{\tau^r}^+ \{x\}(t) := \left(1 + \tau^r \frac{d}{dt}\right) x(t). \quad (2)$$

The time constant τ^r is associated with the neuronal output rate, which, rather than being simply $\varphi(u)$ (with u the membrane potential and φ the neuronal activation function), takes on the prospective form $r = \varphi(\mathcal{D}_{\tau^r}^+ \{u\})$.

In brief, this prospectivity can arise from two distinct mechanisms. On one hand, it follows as a direct consequence of the output nonlinearity [20]. On the other hand, it appears when the neuronal membrane (alternatively but equivalently, its leak potential or firing threshold) is negatively coupled to an additional retrospective variable. Such variables include, for example, the inactivation of sodium channels, or slow adaptation (both spike frequency and subthreshold) currents [21, 22], thus giving neurons access to a wide range of prospective horizons. For a more detailed discussion of prospectivity in neurons with adaptation currents, we refer to Methods Section 6.3. We note that in analog neuromorphic hardware, adaptive neurons are readily available [23–26], but a direct implementation of an inverse low-pass filter would evidently constitute an even simpler and more efficient solution.

Importantly, the retrospective and prospective operators $\mathcal{I}_{\tau^m}^-$ and $\mathcal{D}_{\tau^r}^+$ have opposite effects; in particular, for $\tau^m = \tau^r$, they are exactly inverse, which forms the basis of LE [17]. In that case, the exact inversion of the low-pass filtering allows the network to react instantaneously to a given input, which can solve the relaxation problem for spatial tasks. However, this exact inversion also precludes the use of neurons for explicit temporal processing in spatio-temporal tasks, which represents the main focus of this work.

We can now define the GLE framework as a set of four postulates, from which the entire network structure and dynamics follow. The postulates use these operators to describe how forward and backward prospectivity work in biological neuronal networks. As we will see later, the dynamical equations derived from these postulates approximate the equations derived

from AM/BPTT, but without violating causality, with only local dependencies and without the need for learning phases.

Postulate 1. *The canonical variables describing neuronal network dynamics are $\mathcal{D}_{\tau_i^m}^+ \{u_i(t)\}$ and $\mathcal{D}_{\tau_i^r}^+ \{u_i(t)\}$, where each neuron is denoted with the subscript $i \in \{1, \dots, n\}$.*

This determines the relevant dynamical variables for the postulates below. They represent, respectively, the prospective voltages with respect to the membrane and rate time constants. Importantly, each neuron i can in principle have its own time constants τ_i^x , and the two are independent, so in general $\tau_i^m \neq \tau_i^r$. This is in line with the biological mechanisms for retro- and prospectivity, which are also unrelated, as discussed above.

Postulate 2. *A neuronal network is fully described by the energy function*

$$E(t) = \frac{1}{2} \sum_i \|e_i(t)\|^2 + \beta C(t), \quad (3)$$

where $e_i(t) = \mathcal{D}_{\tau_i^m}^+ \{u_i(t)\} - \sum_j W_{ij} \varphi(\mathcal{D}_{\tau_j^r}^+ \{u_j(t)\}) - b_i$ is the mismatch error of neuron i . W_{ij} and b_i respectively denote the components of the weight matrix and bias vector, φ the output nonlinearity and β a scaling factor for the cost. The cost function $C(t)$ is usually defined as a function of the rate and hence of $\mathcal{D}_{\tau_i^r}^+ \{u_i\}$ of some subset of output neurons.

This approach is inspired by physics and follows a time-honored tradition in machine learning and computational neuroscience [17, 27–29]. Under the weak assumption that the cost function can be factorized, this energy is simply a sum over neuron-local energies $E_i(t) = \frac{1}{2} e_i^2(t) + \beta C_i(t)$. Each of these energies represent a difference between what membrane voltage the neuron predicts for its near future ($\mathcal{D}_{\tau_i^m}^+ \{u_i(t)\}$), and what its functional afferents (and bias) expect it to be ($\sum_j W_{ij} \varphi(\mathcal{D}_{\tau_j^r}^+ \{u_j(t)\}) + b_i$), with the potential addition of a teacher nudging term for output neurons that is related to the cost that the network seeks to minimize ($\beta C_i(t)$).

Postulate 3. *Neuron dynamics follow the stationarity principle*

$$\mathcal{I}_{\tau_i^m}^- \left\{ \frac{\partial E}{\partial \mathcal{D}_{\tau_i^m}^+ \{u_i\}} \right\} + \mathcal{I}_{\tau_i^r}^- \left\{ \frac{\partial E}{\partial \mathcal{D}_{\tau_i^r}^+ \{u_i\}} \right\} = 0. \quad (4)$$

As the two rates of change (the partial derivatives) are with respect to prospective variables, with temporal advances determined by τ^m and τ^r , they can be intuitively thought of as representing quantities that refer to different points in the future – loosely speaking, at $t + \tau^m$ and $t + \tau^r$. To compare the two rates of change on equal footing, they need to be pulled back into the present by their respective inverse operators $\mathcal{I}_{\tau^m}^-$ and $\mathcal{I}_{\tau^r}^-$. It is the equilibrium of this mathematical object, otherwise not immediately apparent (hence: “latent”) from observing the network dynamics themselves (see below), that gives our framework its name. It is also easy to check that for the special case of $\tau_i^m = \tau_i^r \quad \forall i$, GLE reduces to LE [17] – hence the ‘generalized’ nomenclature.

Postulate 4. *Parameter dynamics follow gradient descent*

(GD) on the energy

$$\dot{\theta} = -\eta_{\theta} \frac{\partial E}{\partial \theta} \quad (5)$$

with individual learning rates η_{θ} .

Parameters include $\theta = \{\mathbf{W}, \mathbf{b}, \tau^m, \tau^r\}$, with boldface denoting matrices, vectors, and vector-valued functions. These parameter dynamics are the equivalent of plasticity, both for synapses (W_{ij}) and for neurons (b_i, τ_i^m, τ_i^r). The intuition behind this set of postulates is illustrated in Fig. 2. Without an external teacher, the network is unconstrained and simply follows the dynamics dictated by the input; as there are no errors, both cost C and energy E are zero. As an external teacher appears, errors manifest and the energy landscape becomes positive; its absolute height is scaled by the coupling parameter β . While neuron dynamics $\dot{\mathbf{u}}$ trace trajectories across this landscape, plasticity $\dot{\theta}$ gradually reduces the energy along these trajectories (cf. Fig. 2). Thus, during learning, the energy landscape (more specifically, those parts deemed relevant by the task of the network, lying on the state subspace traced out by the trajectories during training) is gradually lowered, as illustrated by the faded surface. Ultimately, after learning, the energy will ideally be pulled down to zero, thus implicitly also reducing the cost, because it is a positive, additive component of the energy. Beyond this implicit effect, we will show later how the network dynamics derived from these postulates also explicitly approximate gradient descent on the cost.

The four postulates above fully encapsulate the GLE framework. From here, we can now take a closer look at the network dynamics and see how they enable the sought transport of signals to the right place and at the right time.

2.2 Network dynamics

With our postulates at hand, we can now infer dynamical and structural properties of neuronal networks that implement GLE. We first derive the neuronal dynamics by applying the stationarity principle (Postulate 3, Eqn. 4) to the energy function (Postulate 2, Eqn. 3):

$$\tau_i^m \dot{u}_i = -u_i + \sum_j W_{ij} \varphi(\mathcal{D}_{\tau^r}^+ \{u_j\}) + b_i + e_i. \quad (6)$$

This is very similar to conventional leaky integrator dynamics, except for the use of the prospective operator for the neuronal output, which we already connected to the dynamics of biological neurons above. Thus, in the GLE framework, a single neuron performs four operations in the following order: (weighted) sum of presynaptic inputs, integration (retrospective), differentiation (prospective), and the output nonlinearity. The timescale associated with retrospectivity is the membrane time constant τ^m , whereas prospectivity is governed by τ^r . This means that even if the membrane time constant is fixed, as may be the case for certain neuron classes or models thereof, single neurons can still tune the time window to which they attend by adapting their prospectivity. This temporal attention window can lie in the past (retrospective neurons, $\tau^r < \tau^m$), in the present (instantaneous neurons, $\tau^r = \tau^m$, as described by LE), but also in the future (prospective neurons, $\tau^r > \tau^m$). These neuron classes can, for example, be found in

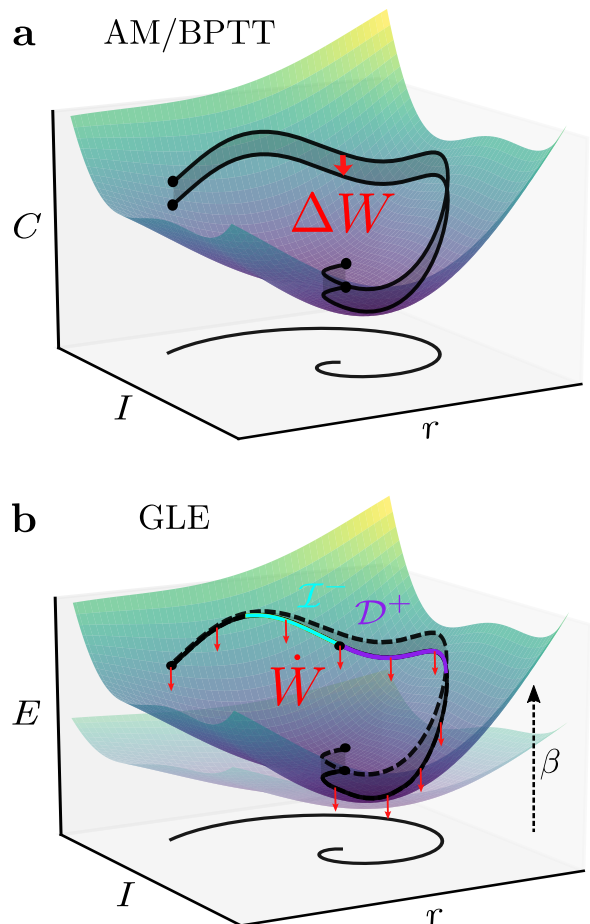


Figure 2: Comparison between AM and GLE. Network dynamics define trajectories (black) in the cost/energy landscape, spanned by external inputs I and neuron outputs r . Parameter updates (red, here: synaptic weights) reduce the cost/energy along these trajectories. **(a)** AM records the trajectory between two points in time and calculates a (macroscopic) update ΔW that reduces the *integrated* cost along this trajectory. **(b)** GLE calculates an approximate cost gradient *at every point in time*, by taking into account past network states (via retrospective coding, \mathcal{I}_{τ^-}) and estimating future errors from the current state (via prospective coding, \mathcal{D}_{τ^+}). Learning is thus fully online and can gradually reduce the energy in real-time, with the real trajectory slowly diverging from the (virtual) trajectory of the network when learning is turned off (dashed line).

cortex [30, 31] and hippocampus [32, 33]; for a corresponding modeling study, we refer to [22]. The prospective capability becomes essential for error propagation, as we discuss below, while the use of different attention windows allows the learning of complex spatio-temporal patterns, as we show in action in Section 3. Note that for $\tau^r = 0$, we recover classical leaky integrator neurons as a special case of our framework.

Eqn. 6 also suggests a straightforward interpretation of neuronal morphology and its associated functionality. In particular, it suggests that separate neuronal compartments store different variables: a somatic compartment for the voltage u_i , and two dendritic compartments for integrating $\sum_j W_{ij} r_j$ and e_i , respectively. This separation also gives synapses access to these quantities, as we discuss later on. Further below, we also show how this basic picture extends to a microcircuit for learning and adaptation in GLE networks.

The error terms in GLE also naturally include prospective and retrospective operators. As stated in Postulate 2 (Eqn. 3), the

total energy of the system is a sum over neuron-local energies. If we now consider a hierarchical network, these terms can be easily rearranged into the form (see Methods and SI, Section 9)

$$\mathbf{e}_\ell = \mathcal{D}_{\tau_\ell^+}^+ \left\{ \mathcal{I}_{\tau_\ell^-}^- \left\{ \varphi'_\ell \circ \mathbf{W}_{\ell+1}^T \mathbf{e}_{\ell+1} \right\} \right\}, \quad (7)$$

where ℓ denotes the network layer and φ' denotes the derivative of φ evaluated at $\mathcal{D}_{\tau_\ell^+}^+ \{\mathbf{u}_\ell\}$. In this form, the connection to backpropagation (BP) algorithms becomes apparent. For $\tau^r = \tau^m$, the operators cancel and Eqn. 7 reduces to the classical (spatial) error backpropagation algorithm, as already studied in [17]. When $\tau^r \neq \tau^m$ however, the error exhibits a switch between the two time constants when compared to the forward neuron dynamics (Eqn. 6): whereas forward rates are retrospective with τ^m and prospective with τ^r , backward errors invert this relationship. In other words, backward errors invert the temporal shifts induced by forward neurons. As we discuss in the following section, it is precisely this inversion that enables the approximation of AM/BPTT.

As for the neuron dynamics, parameter dynamics also follow from the postulates above. For example, synaptic plasticity is obtained by applying the gradient descent principle (Postulate 4, Eqn. 5 with respect to synaptic weights \mathbf{W}) to the energy function (Postulate 2, Eqn. 3):

$$\dot{W}_{ij} = \eta_W e_i r_j = \eta_W (\mathcal{D}_{\tau^m}^+ \{u_i\} - v_i) r_j, \quad (8)$$

where $v_i = \sum_j W_{ij} r_j$ is the membrane potential of the dendritic compartment that integrates bottom-up synaptic inputs. Such three-factor error-correcting rules have often been discussed in the context of biological deep learning (see [34] for a review). For a more detailed biological description of our specific type of learning rule, we refer to [35]. Notice that parameter learning is neuron-local, and that we are performing gradient descent explicitly on the energy E , and only implicitly on the cost C . This is a quintessential advantage of the energy-based formalism, as the locality of GLE dynamics is a direct consequence of the locality of the postulated energy function. This helps provide the physical and biological plausibility that other methods lack. In Section 2.4, we discuss how GLE dynamics relate to physical neuronal networks and cortical circuits, but first, we show how these dynamics effectively approximate AM/BPTT.

2.3 GLE dynamics implement a real-time approximation of AM/BPTT

The learning capabilities of GLE arise from the specific form of the errors encapsulated in the neuron dynamics, which make the similarity to AM/BPTT apparent, as discussed below. For a detailed derivation of the following relationships, we refer to the Methods Section 6.2 and the Supplement Section 9.

Just like in GLE, learning in AM/BPTT is error-correcting:

$$\Delta \mathbf{W}_\ell^{\text{AM}} = \int_0^T \boldsymbol{\lambda}_\ell \mathbf{r}_{\ell-1}^T dt, \quad (9)$$

where the continuous-time adjoint variables $\boldsymbol{\lambda}$ in AM are equivalent to the time-discrete errors in BPTT. While typically calculated in reverse time, as for the backpropagated errors in

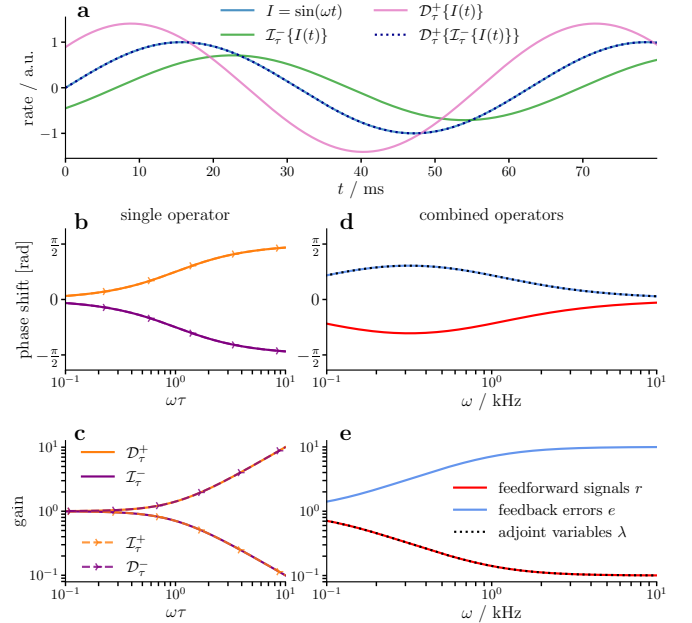


Figure 3: Comparison of GLE and AM/BPTT in Fourier space. (a) Effect of the individual and combined GLE operators \mathcal{I}_{τ^-} and \mathcal{D}_{τ^+} with shared time constant τ on a single frequency component of an input current I . \mathcal{I}_{τ^-} generates a negative phase shift (towards later times) and sub-unit gain. \mathcal{D}_{τ^+} is its exact inverse and generates a positive phase shift (towards earlier times) and supra-unit gain. (b) Phase shift and (c) gain of all four temporal operators in GLE and AM/BPTT across a wide range of the frequency spectrum. Note how the prospective operators \mathcal{D}_{τ^+} and \mathcal{I}_{τ^+} (orange) have the same shift but inverse gain; the same holds for the retrospective operators \mathcal{I}_{τ^-} and \mathcal{D}_{τ^-} (purple). (d) Phase shift and (e) gain of the combined operators as they appear in the neuron dynamics. Here, we choose an example forward neuron (blue) with a retrospective attention window ($\tau^m > \tau^r$). Both the associated GLE errors e (blue) and the AM/BPTT adjoint variables λ (dotted) are prospective and precisely invert this phase shift, albeit with a different gain.

BPTT, for the specific dynamics of cost-decoupled GLE networks ($\beta = 0 \Rightarrow \mathbf{e} = \mathbf{0} \Rightarrow E = 0$) it is possible to write the adjoint dynamics in forward time as follows:

$$\boldsymbol{\lambda}_\ell = \mathcal{I}_{\tau_\ell^m}^+ \left\{ \mathcal{D}_{\tau_\ell^-}^- \left\{ \varphi'_\ell \circ \mathbf{W}_{\ell+1}^T \boldsymbol{\lambda}_{\ell+1} \right\} \right\}. \quad (10)$$

Here, we use adjoint operators $\mathcal{D}_{\tau^-}^- \{x(t)\} = (1 - \tau \frac{d}{dt}) x(t)$ and $\mathcal{I}_{\tau^+}^+ \{x(t)\} = \frac{1}{\tau} \int_t^\infty x(s) e^{\frac{t-s}{\tau}} ds$ to describe the hierarchical coupling of the adjoint variables. We note that the adjoint dynamics (Eqn. 10) can also be derived in our GLE framework by simply replacing $\mathcal{I}_{\tau_\ell^m}^-$ with $\mathcal{D}_{\tau_\ell^m}^-$ in Postulate 3.

Note the obvious similarity between Eqns. 7 and 10. The inner term $\varphi'_\ell \circ \mathbf{W}_{\ell+1}^T \boldsymbol{\lambda}_{\ell+1}$ is identical and describes backpropagation through space. The outer operators perform the temporal backpropagation, enacting the exact opposite temporal operations compared to the representation neurons (first retrospective with τ^r then prospective with τ^m , cf. Eqn. 6).

However, there is a subtle but important difference between the temporal operators in GLE and AM/BPTT. In AM/BPTT, the retrospective operator is differential and the prospective one is integral. It is this integral operator $\mathcal{I}_{\tau^m}^+$ that causes AM/BPTT to be noncausal, as it assumes a knowledge of the future that is impossible to calculate in an online fashion.

How GLE can perform an online approximation of this operation is best seen in frequency space, where we can analyze how the combined temporal operators affect individual Fourier components (see also Fig. 3). For a single such component – a sine wave input of fixed angular frequency ω – each operator causes a temporal (phase) shift: the retrospective operator \mathcal{I}_τ^- causes a shift of the input signal towards later times, while the prospective operator causes an inverse shift towards earlier times. These phase shifts are exactly equal to those generated by the adjoint operators \mathcal{D}_τ^- and \mathcal{I}_τ^+ . Therefore, in terms of temporal shift, the GLE errors are perfect replicas of the adjoint variables derived from exact gradient descent; this is the most important part of the temporal backpropagation in AM.

In terms of gain, GLE and AM/BPTT are inverted. For smaller angular frequencies $\omega\tau \lesssim 1$, this approximation is very good and the gradients are only weakly distorted. We will later see that in practice, for hierarchical networks with sufficiently diverse time constants, successful learning does not strictly depend on this formal requirement. What appears more important is that, even for larger $\omega\tau$, GLE errors always conserve the sign of the correct adjoints, so the error signal always remains useful; moreover, higher-frequency oscillations in the errors tend to average out over time, as we demonstrate in simulations below.

2.4 Cortical / neuromorphic circuits

As shown above, GLE backward (error) dynamics engage the same sequence of operations as those performed by forward (representation) dynamics: first integration \mathcal{I}_τ^- , then differentiation \mathcal{D}_τ^+ . This suggests that backward errors can be transmitted by the same type of neurons as forward signals [36, 37], which is in line with substantial experimental evidence that demonstrates the encoding of errors in L2/3 pyramidal (PYR) neurons [38–43]. Note that correct local error signals are only possible with neurons that are capable of both retrospective (\mathcal{I}_τ^-) and prospective (\mathcal{D}_τ^+) coding – the core element of the GLE framework.

This symmetry between representation and error suggests a simple microcircuit motif that repeats in a ladder-like fashion, with L2/3 PYR error neurons counterposing L5/6 PYR representation neurons (Fig. 4). Information transmitted between the two streams provides these neurons with all the necessary local information to carry out GLE dynamics. In particular, error neurons can elicit the representation of corresponding errors in dendritic compartments of representation neurons, allowing forward synapses to access and correct these errors through local plasticity. Recent evidence for error representation in apical dendrites provides experimental support for this component of the model [44].

The correct propagation of errors requires two elements that can be implemented by static lateral synapses. First, error neuron input needs to be multiplicatively gated by the derivative of the corresponding representation neuron’s activation function φ . This can either happen through direct lateral interaction, or through divisive (dis)inhibition, potentially carried out by somatostatin (SST) and parvalbumin (PV) interneuron populations [45–48], via synapses that are appropriately

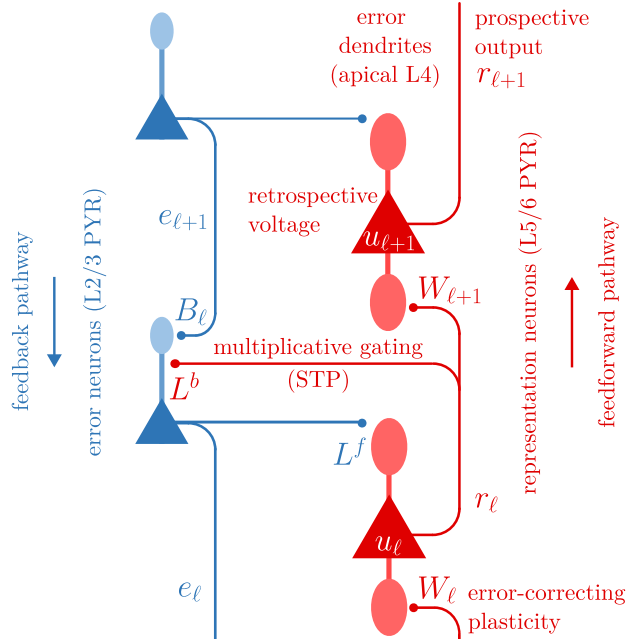


Figure 4: Microcircuit implementation of GLE: key components. Representation neurons form the forward pathway (red), error neurons form the backward pathway (blue). Both classes of neurons are PYR, likely located in different layers of cortex. Lateral connections enable information exchange and gating between the two streams. The combination of retrospective membrane and prospective output dynamics allow these neurons to tune the temporal shift of the transmitted information. Errors are also represented in dendrites, likely located in the apical tuft of signal neurons, enabling local three-factor plasticity to correct the backpropagated errors.

positioned at the junction between dendrites and soma. The required signal φ' can be generated and transported in different ways depending on the specific form of the activation function. For example, if $\varphi = \text{ReLU}$, lateral weights can simply be set to $L^b = 1$. For sigmoidal activation functions, φ' can be very well approximated by synapses with short-term plasticity (e.g., [49], Eqn. 2.80). The second requirement regards the communication of the error back to the error dendrites of the representation neurons; this is easily achieved by setting $L^f = 1$.

Ideally, synapses responsible for error transport in the feedback pathway need to mirror forward synapses: $B = W^T$ (cf. Eqn. 7). While this can, to some extent, be mitigated by feedback alignment [50], improved solutions to the weight transport problem that are both online and local have also been recently proposed [51, 52].

3 Applications

In this section, we demonstrate several applications of the GLE framework. We first illustrate its operation in small-scale examples, to provide an intuition of how GLE networks can learn to solve non-trivial temporal tasks. Later on, we discuss more difficult problems that usually require the use of sophisticated deep learning methods and compare the performance of GLE with the most common approaches used for these problems in machine learning.

3.1 GLE in a chain of neurons

As a first application, we study learning in a forward chain of two neurons provided with a periodic step function input (Fig. 5). To make the target learnable, we use a network with the same architecture but different (fixed) parameters as a teacher. To better illustrate the difficulty of temporal credit assignment, we choose relatively long time constants for the teacher network in comparison with the oscillations in the network input. The task of the student network is to mimic the output of the teacher by adapting its own forward weights and membrane time constants. We compare three different solutions to this problem: (1) a GLE network with time-continuous dynamics, including synaptic and neuronal plasticity; (2) standard error backpropagation using instantaneous error signals $e_i = \varphi'_i w_i e_{i+1}$; (3) truncated BPTT through the discretized neuron dynamics using PyTorch’s `autograd` functionality for different truncation windows.

We first note that the GLE network learns the task successfully and quickly, in contrast to instantaneous backpropagation. To understand why, it is particularly instructive to compare its errors to the instantaneous ones in a scenario where the time constants of the signal neurons are correct, but their input weights are not (Fig. 5b, left). The instantaneous errors are always in sync with the output error, but their shape and timing become increasingly desynchronized from the neuronal inputs as they propagate toward the beginning of the chain, because they do not take into account the lag induced by the representation neurons. Thus, the correct temporal coupling between errors and presynaptic rates required by plasticity (cf. Eqn. 8, see also Eqns. 12 to 15 in the Methods) is corrupted and learning is impaired. Note that instantaneous errors are already a strong assumption and themselves require a form of prospectivity [17]; without any prospectivity, learning performance would be even more drastically compromised. In contrast, the GLE errors gradually shift forward in time, matching the phase and shape of the respective neuronal inputs, and thus allowing the stable learning of all network parameters, weights and time constants alike.

Here, we can also see an advantage of GLE over the classical BPTT solution (Fig. 5c). Despite only offering an approximation of the exact gradient calculated by BPTT, it allows learning to operate continuously, fully online. As discussed above, BPTT needs to record a certain period of activity before being able to calculate parameter updates. If this truncation window is too short, it fails to capture longer transients in the input and learning stalls or diverges (brown and pink, respectively). Only with a sufficiently long truncation window does BPTT converge to the correct solution (orange), but at the cost of potentially exploding gradients and/or slower convergence due to the resulting requirement of reduced learning rates.

3.2 Credit assignment in small GLE networks

To better visualize how errors are computed and transmitted in more complex GLE networks, we now consider a teacher/student setup with two hidden layers, each with one instantaneous and one retrospective neuron (Fig. 6a). Through this combination of fast and slow pathways between network in-

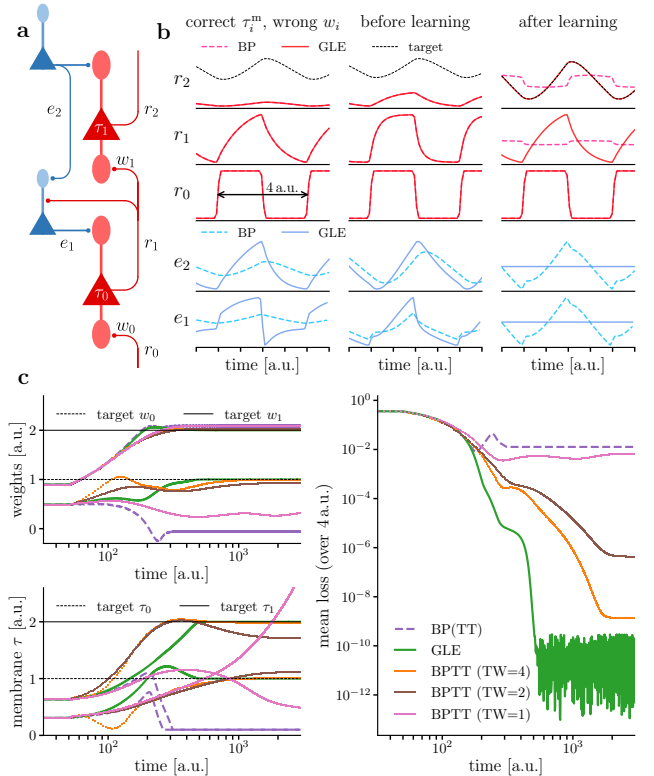


Figure 5: Learning with GLE in a simple chain. (a) Network setup. A chain of two retrospective representation neurons (red) learns to mimic the output of a teacher network (identical architecture, different parameters). In GLE, this chain is mirrored by a chain of corresponding error neurons (blue), following the microcircuit template in Fig. 4. We compare the effects of three learning algorithms: GLE (green), backpropagation with instantaneous errors (purple) and BPTT (point markers denote the discrete nature of the algorithm; pink, brown and orange denote different truncation windows (TW)). (b) Output of representation neurons (r_i , red) and error neurons (e_i , blue) for GLE and instantaneous backpropagation. Left: correct membrane time constants but wrong weights. Middle: before learning (i.e., both weights and membrane time constants are wrong). Right: after learning. (c) Evolution of weights, time constants and overall loss. Fluctuations at the scale of 10^{-10} are due to limits in the numerical precision of the simulation.

put and output, such a small setup can already perform quite complex transformations on the input signal (Fig. 6b). From the perspective of learning an input-output mapping, this can be stated as the output neuron having access to multiple time scales of the input signal, despite the input being provided to the network as a constant stream in real time. This is essential for solving the complex classification problems that we describe later.

To isolate the effect of error backpropagation into deeper layers, we keep all but the bottom weights fixed and identical between teacher and student. We then compare error dynamics and learning in the GLE network with exact gradient descent on the cost as computed by AM/BPTT.

While both methods converge to the correct target (Fig. 6b and e), they don’t necessarily do so at the same pace, since AM/BPTT cannot perform online updates, as also discussed above. Also, GLE error propagation is only identical to the coupling of adjoint variables (AM/BPTT) for instantaneous neurons with $\tau^m = \tau^r$ ($e_1^i = \lambda_1^i$). In general, this is not the case ($e_1^i \neq \lambda_1^i$), as GLE errors tend to overemphasize higher

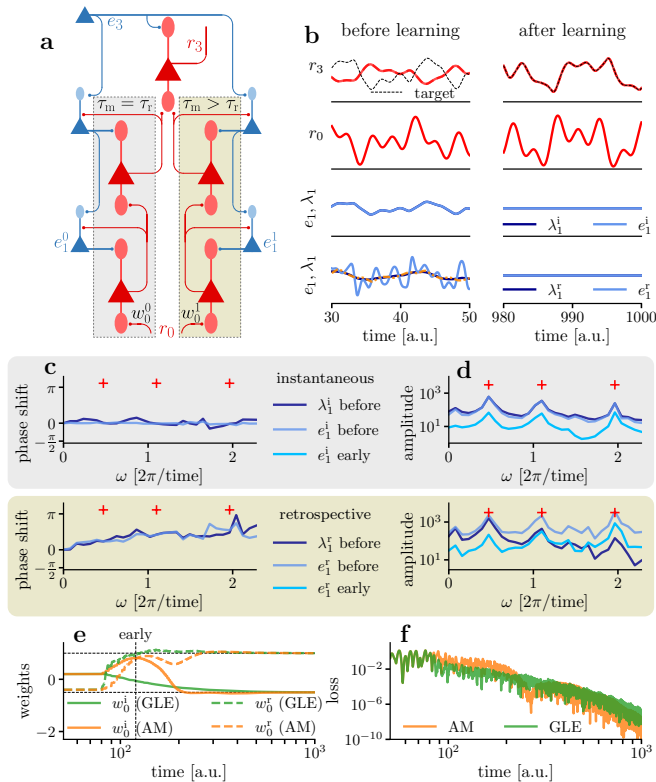


Figure 6: Error propagation and learning with GLE in a small hierarchical network. (a) Network setup. A network with one output neuron and two hidden layers (red) learns to mimic the output of a teacher network (identical architecture, different input weights to the first hidden layer). Each hidden layer contains one instantaneous ($\tau = \tau^r = 1$) and one retrospective ($\tau^m = 1, \tau^r = 0.1$) neuron. In GLE, the corresponding error pathway (blue) follows the microcircuit template in Fig. 4. The input is defined by a superposition of three angular frequency components $\omega \in \{0.49, 1.07, 1.98\}$. Here, we compare error propagation, synaptic plasticity and ultimately the convergence of learning under GLE and AM. (b) Input and output rates (r , red), along with bottom layer errors (e , light blue) and adjoints (λ , dark blue) before and during the late stages of learning. A running average over e is shown in orange. (c) Phase shifts (compared to the output error e_3) and (d) amplitudes of bottom layer errors and adjoints across a wide range of their angular frequency spectrum. Top: e_1^i and λ_1^i for the instantaneous neuron. Bottom: e_1^r and λ_1^r for the retrospective neuron. Note that due to the nonlinearity of neuronal outputs, the network output has a much broader distribution of frequency components compared to the input (with its three components highlighted by the red crosses). Error amplitudes are shown at two different moments during learning. (e) Evolution of the bottom weights (w_0^i, w_0^r) and (f) of the loss during learning. The vertical dashed lines mark the snapshots at which adjoint and error spectra are plotted above.

frequency components in the signal (cf. also Section 2.3 and Fig. 6d). However, this only occurs for slow, retrospective neurons, which only need to learn the slow components of the output signal. For sufficiently small learning rates, plasticity in their afferent synapses effectively integrates over these oscillations and lets them adapt to the relevant low-frequency components. Indeed, the close correspondence to AM/BPTT is reflected in the average GLE errors, which closely track the corresponding adjoints. While it was not necessary to make use of such additional components in our simulations, high-amplitude high-frequency oscillations in the error signals could be mitigated by several simple mechanisms, including saturating activation functions for the error neurons, input averaging in the error dendrites or synaptic filtering of the plasticity signal.

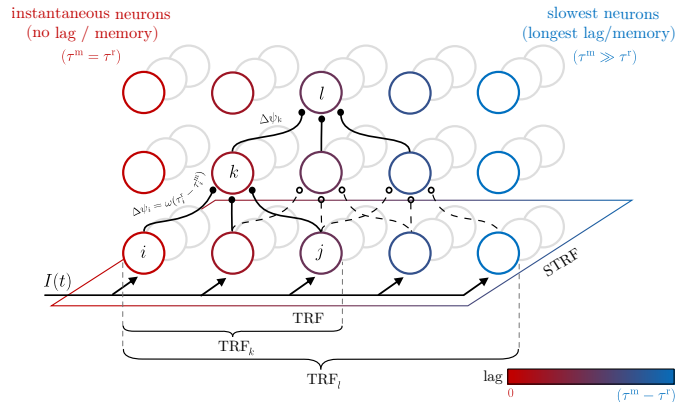


Figure 7: Neuronal diversity fosters complex temporal attention windows in GLE networks. In the simplest case, a single input signal $I(t)$ is fed into a GLE network and all neurons in the bottom layer have access to the same information stream. However, the output of each neuron generates a temporal shift, depending on its time constants τ^m and τ^r (as highlighted by the neuron colors). Different chains of such neurons thus provide neurons in higher levels of the hierarchy with a set of attention windows across the past input activity. Synaptic and neuronal adaptation shape the nature of these temporal receptive fields (TRFs). For multidimensional input, neuron populations (gray) encode the additional spatial dimension and neuronal receptive fields become spatiotemporal (STRFs).

Following the analysis in Section 2.3, our simulations now demonstrate how GLE errors encode the necessary information for effective learning. Most importantly, GLE errors and adjoint variables (AM/BPTT) have near-identical timing, as shown by the alignment of their phase shifts across the signal frequency spectrum (Fig. 6c). Moreover, for the errors of the retrospective neurons, these phase shifts are positive with respect to the output error, thus demonstrating the prospectivity required for the correct temporal alignment of inputs and errors. The amplitudes of e and λ also show distinct peaks at the same angular frequencies, corresponding to the three components of the input signal that need to be mapped to the output (Fig. 6d). These signals can thus guide plasticity in the correct direction, gradually learning first the slow and then the fast components of the input-output mapping. This is also evinced by Fig. 6e, where the input weights of the retrospective neurons w_0^r are the first to converge. The ensuing reduction of the slow error components provides the input weights of the instantaneous neurons w_0^i with cleaner access to the fast error components – the only ones that they can actually learn – which allows them to converge as well.

3.3 GLE for challenging spatio-temporal classification problems

We now demonstrate the performance of GLE in larger hierarchical networks, applied to difficult spatio-temporal learning tasks, and compare it to other solutions from contemporary machine learning. An essential ingredient for enabling complex temporal processing capabilities in GLE networks is the presence of neurons with diverse time constants τ^m and τ^r (Fig. 7). Each of these neurons can be intuitively viewed as implementing a specific temporal attention window, usually lying in the past, proportionally to $\tau^m - \tau^r$. More specifically, for a given angular frequency component of the input ω , this window is centered around a phase shift of

$\arctan(\omega\tau^r) - \arctan(\omega\tau^m) \approx \omega(\tau^r - \tau^m)$ for $\omega\tau \lesssim 1$ (cf. Methods Section 6.2). By connecting to multiple presynaptic partners in the previous layer, a neuron thus carries out a form of temporal convolution, similarly to temporal convolutional networks (TCNs) [53]. Deeper networks also allow longer chains of such neurons to be formed, thus providing the output with a diverse set of complex transforms on different time intervals distributed across the past values of the input signal. GLE effectively enables deep networks to learn a useful set of such transforms.

3.3.1 MNIST-1D

We first consider the MNIST-1D [54] benchmark (Fig. 8d) for temporal sequence classification. Other than the name itself and the number of classes, MNIST-1D bears little resemblance to its classical namesake. Here, each sample is a one-dimensional array of points, which can be streamed as a temporal sequence into the network. This deceptively simple setup entails two difficult challenges. First, only 1/4 of each sample contains meaningful information; this chunk is positioned randomly within the sample, every time at a different position. Second, independent noise is added on top of every sample at multiple frequencies, which makes it difficult to remove by simple filtering. To allow a direct comparison between the different algorithms, we use no preprocessing in our simulations.

We first note that a multi-layered perceptron fails to appropriately learn to classify this dataset, reaching a validation accuracy of only around 60%. This is despite the perceptron having access to the entire sequence from the sample at the same time, unrolled from time into space. This highlights the difficulty of the MNIST-1D task. More sophisticated machine learning methods yield much better results, with TCNs [53] and gated recurrent units (GRUs) [55] achieving averages of over 90%. Notably, both of these methods work offline, with TCNs in particular requiring a mapping of temporal signals to spatial representations beforehand, and GRUs requiring offline BPTT training with direct access to the full history of the network.

While offline methods can only update their parameters after the entire sequence has been processed, GLE networks update their parameters in real time. This advantage also presents them with a greater challenge when faced with short informative signals embedded in a sea of noise, for which the target is always on, even in the absence of meaningful information. Since only a fraction of each input actually contains a meaningful signal, GLE networks must be capable of remembering these informative combinations of inputs and targets throughout the uninformative portions of their training. This manifests as an increase in convergence time, but not in ultimate performance, as GLE maintains an overall good online approximation of the true gradients for updating the network parameters. Thus, despite facing a significantly more difficult task compared to the methods that have access to the full network activity unrolled in time, GLE achieves highly competitive classification results.

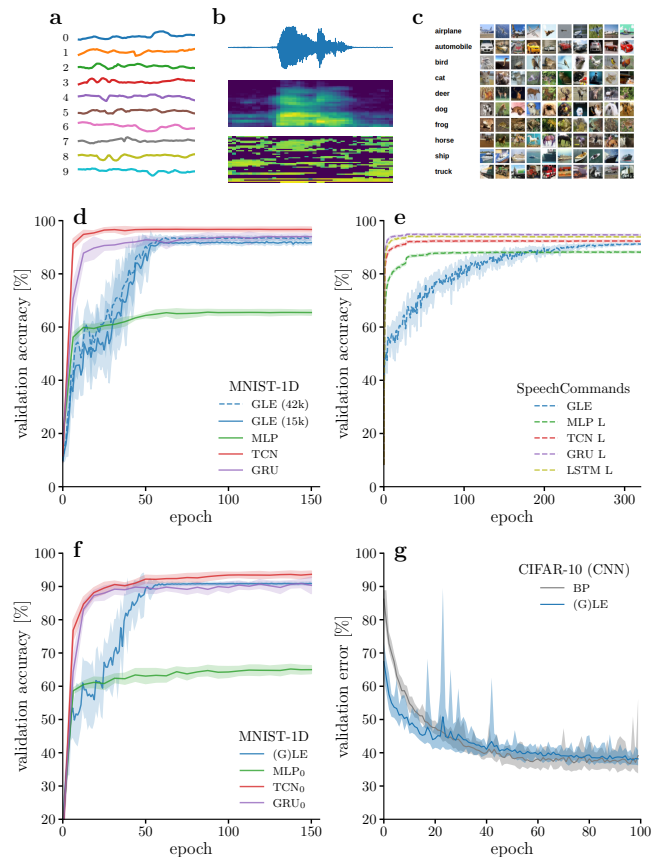


Figure 8: GLE for challenging spatio-temporal classification problems. Averages and standard deviations measured over 5 seeds. Top row: samples from the (a) MNIST-1D, (b) Google Speech Commands (GSC) – including raw and preprocessed input – and (c) CIFAR-10 datasets. (d) Performance of various algorithms on MNIST-1D. Here, we used a higher temporal resolution for the input than in the original reference [54]. (e) Performance of various algorithms on GSC. (f) Performance of a (G)LE LagNet architecture on MNIST-1D. For reference, we also show the original results from [54] denoted with the index 0. (g) Performance of a (G)LE convolutional network on CIFAR-10 (taken from [17]) and comparison with backpropagation.

3.3.2 Google Speech Commands

To simultaneously validate the spatial and temporal learning capabilities of GLE, we now apply it to the GSC dataset [56]. This dataset consists of 105'829 one-second long audio recordings of 35 different speech commands, each spoken by thousands of people. In the v2.12 version of this dataset, the usual task is to classify 10 different speech commands in addition to a silence and an unknown class, which comprises all remaining commands. The raw audio signal is transformed into a sequence of 41 Mel-frequency spectrogramss (MFSs); this sequence constitutes the temporal dimension of the dataset and is streamed to the network in real-time. Each of these spectrograms has 32 frequency bins, which are presented as 32 separate inputs to the network, thus constituting the spatial dimension of the dataset.

Fig. 8c compares the performance of GLE to several widely used references: multi-layer perceptron (MLP), TCN, GRU (as used for MNIST-1D) and, additionally, long short-term memory (LSTM) networks [57] – all trained with a variant of backpropagation. Similarly to the MNIST-1D dataset, the

GLE network is trained online, while the reference networks can only be trained offline; furthermore, the MLP and TCN networks do not receive the input as a real-time stream, but rather as a full image, by mapping the temporal dimension onto an additional spatial one. As with MNIST-1D, we see how our GLE networks surpass the MLP baseline and achieve a performance that comes very close to the other references. We thus conclude that, while offering clear advantages in terms of biological plausibility and online learning capability, GLE remains competitive in terms of raw task performance. We also note that, in contrast to the reference baselines, GLE achieves these results without additional tricks such as batch or layer normalization, or the inclusion of dropout layers.

3.3.3 From time to space

The above results explicitly exploit the temporal aspects of GLE and its capabilities as an online approximation of AM/BPTT. However, GLE also contains purely spatial back-propagation as a subcase, and the presented network architecture can lend itself seamlessly to spatial tasks such as image classification. In cases like this, where temporal information is irrelevant, one can simply take the LE limit of GLE by setting $\tau^m = \tau^r$ for all neurons in the network [17]. In the following, we demonstrate these capabilities in two different scenarios. Note that GLE learns in a time-continuous manner in all of these cases as well, with the input being presented in real-time.

First, we return to the MNIST-1D dataset, but adapt the network architecture as follows. The 1D input first enters a non-plastic preprocessing network module consisting of several parallel chains of retrospective neurons. The neurons in each chain are identical, but different across chains: the fastest chain is near-instantaneous with $\tau^m \rightarrow 0$, while the slowest chain induces a lag of about 1/4 of the total sample length. The endpoints of these chains constitute the input for a hierarchical network of instantaneous neurons ($\tau^m = \tau^r$). By differentially lagging the input stream along the input chains, this configuration approximately maps time to space (the output neurons of the chains). This offers the hierarchical network access to a sliding window across the input – hence the acronym “LagNet” for this architecture – and changes the nature of the credit assignment problem from temporal to spatial. While the synaptic weights in the chains are fixed, those in the hierarchical network are trained with GLE, which in this scenario effectively reduces to LE. As shown in Fig. 8f, GLE is capable of training this network to achieve competitive performance with the reference methods discussed above.

As a second application to purely spatial problems, we focus on image classification. Since GLE does not assume any specific connectivity pattern, we can adapt the network topology to specific use cases. In Fig. 8g we demonstrate this by introducing convolutional architectures (LeNet-5 [58]) and applying them to the CIFAR10 [59] dataset. With test errors of $(38.0 \pm 1.3)\%$, GLE is again on par with ANNs with identical structure at $(39.4 \pm 5.6)\%$. We therefore conclude that, as an extension of LE, GLE naturally maintains its predecessor’s competitive capabilities for online learning of spatial tasks.

4 Discussion

We have presented GLE, a novel framework for spatio-temporal computation and learning in physical neuronal networks. Inspired by well-established approaches in theoretical physics, GLE derives all laws of motion from first principles: a global network energy, a conservation law and a dissipation law. Unlike more traditional approaches, which aim to minimize a cost defined only on a subset of output neurons, our approach is built around an energy function which connects all relevant variables and parameters of all neurons in the network. This permits a unified view on the studied problem and creates a tight link between the dynamics of computation and learning in the neuronal system. The extensive nature of the energy function (i.e., its additivity over subsystems) also provides an important underpinning for the locality of the derived dynamics.

In combination, these dynamics ultimately yield a local, online, real-time approximation of AM/BPTT – to our knowledge, the first of its kind. Moreover, they suggest a specific implementation in physical neuronal circuits, thus providing a possible template for spatio-temporal credit assignment in the brain, as well as blueprints for dedicated hardware implementations. This shows that, in contrast to conventional wisdom, physical neuronal networks can implement future-facing algorithms for temporal credit assignment. More recently, tentative calls in this direction have indeed been formulated [12], to which GLE provides an answer.

In the following, we highlight some interesting links to other models in machine learning, discuss several biological implications of our model, and suggest avenues for improvement and extension of our framework.

4.1 Connection to related approaches

Latent Equilibrium (LE) As the spiritual successor of LE [17], GLE inherits its energy-based approach, as well as the derivation of dynamics from energy conservation and minimization. GLE also builds on the insight from LE that prospective coding can undo the low-pass filtering of neuronal membranes. The core addition of GLE lies in the separation of prospective and retrospective coding, leading to an energy function that depends on two types of canonical variables instead of just one, and to a conservation law that accounts for their respective time scales. The resulting neuron dynamics can thus have complex dependencies on past and (estimated) future states, whereas information processing in LE is always instantaneous. Functionally, this allows neurons to access their own past and future states (through appropriate prospective and retrospective operators), thereby allowing the network to minimize an integrated cost over time, whereas LE only minimizes an instantaneous cost.

Because LE can be seen as a limit case of GLE, the new framework offers a more comprehensive insight into the effectiveness of its predecessor, and also answers some of the questions left open by the older formalism. Indeed, the GLE analysis demonstrates that LE errors are an exact implementation of the adjoint dynamics of the forward system for equal time con-

stants, further confirming the solid grounding of the method, and helping explain its proven effectiveness. Conversely, GLE networks can learn to evolve towards LE via the adaptation of time constants if required by the task to which the framework is applied. While LE also suggests a possible mechanism for learning the coincidence of time scales, GLE provides a more versatile and rigorous learning rule that follows directly from the first principles on which the framework is based. More generally speaking, by having access to local plasticity for all parameters in the network, GLE networks can either select (through synaptic plasticity) or adapt (through neuronal plasticity) neurons and their time constants in order to achieve their target objective.

Thus, GLE not only extends LE to a much more comprehensive class of problems (spatio-temporal instead of purely spatial), but also provides it with a better theoretical grounding, and with increased biological plausibility.

Neuronal least-action (NLA) Similarly inspired by physics, but following a different line of thought, the NLA principle [60] also uses prospective dynamics as a core component. It uses future discounted membrane potentials $\tilde{u} = \mathcal{I}_{\tau_m}^+ \{u\}$ as canonical variables for a Lagrangian L and derives neuronal dynamics as associated Euler-Lagrange equations. A simpler but equivalent formulation places NLA firmly within the family of energy-based models such as LE and GLE, where L is replaced by an equivalent energy function E that sums over neuron-local errors and from which neuronal dynamics can be derived by applying the conservation law $\mathcal{D}_{\tau_m}^+ \{\partial E / \partial u\} = 0$.

The most important difference to GLE is that NLA cannot perform temporal credit assignment. Indeed, other than imposing a low-pass filter on its inputs, an NLA network effectively reacts instantaneously to external stimuli and can neither carry out nor learn temporal sequence processing. This is an inherent feature of the NLA framework, as the retrospective low-pass filter induced by each neuronal membrane exactly undoes the prospective firing of its afferents.

This property also directly implies that, except for the initial low-pass filter on the input, all neurons in the network need to share a single time constant for both prospective and retrospective dynamics. In contrast, both LE and GLE successively lift this strong entanglement by modifying the energy function and conservation law. LE correlates retro- and prospectivity within single neurons and allows their matching to be learned, thus obviating the need for globally shared time constants, while GLE decouples these two mechanisms, thus enabling temporal processing and learning, as discussed above.

RTRL and its approximations RTRL [61] is a past-facing algorithm that implements online learning by recursively updating a tensor M_{ijk} that takes into account the influence of every synapse w_{jk} on every neuronal output r_i in the network. As evident from the dimensionality of this object, this requires storing $\mathcal{O}(N^3)$ floating-point numbers in memory (where N is the number of neurons in the network). Because this is much less efficient than future-facing algorithms, RTRL is rarely used in practice, and the manifest non-locality of the influ-

ence tensor also calls into question its biological plausibility. Nonetheless, several approximations of RTRL have been recently proposed, with the aim of addressing these issues [16].

A particularly relevant algorithm of this kind is random feedback online learning (RFLO) [62], in which a synaptic eligibility trace is used as a local approximation of the influence tensor, at the cost of ignoring dependencies between distant neurons and synapses. With a reduced memory scaling of $\mathcal{O}(N^2)$, this puts RFLO at significant advantage over RTRL, while closing the distance to BPTT (with $\mathcal{O}(NT)$, where T is the length of the learning window). In its goal of reducing the exact, but nonlocal computation of gradients to an approximate, but local solution, RFLO shares the same spirit as GLE. In the following, we highlight several important differences which we consider to give GLE both a conceptual and a practical advantage.

First, the neuron membranes and synaptic eligibilities in RFLO are required to share time constants, in order for the filtering of the past activity to be consistent between the two. In cortex, this would imply the very particular neurophysiological coincidence of synaptic eligibility trace biochemistry closely matching the leak dynamics of efferent neuronal membranes. In contrast, the symmetry requirements of GLE are between neurons of the same kind (PYR cells), which share their fundamental physiology, and whose time constants can be learned locally within the framework of GLE.

Second, the dimensionality reduction of the influence tensor proposed by RFLO also puts it at a functional disadvantage, because the remaining eligibility matrix only takes into account first-order synaptic interactions between directly connected neurons. This is in contrast to GLE, which can propagate approximate errors throughout the entire network. This flexibility also allows GLE to cover applications over multiple time scales, from purely spatial classification to slow temporal signal processing. Moreover, GLE accomplishes this within a biologically plausible, mechanistic model of error transmission, while admitting a clear interpretation in terms of cortical microcircuits. Finally, GLE's additional storage requirements only scale linearly with N (one error per neuron at any point in time), which is even more efficient than BPTT.

While both RFLO and GLE are inspired by and dedicated to physical neuronal systems, both biological and artificial, it might still be interesting to also consider their computational complexity for digital simulation, especially given the multitude of digital neuromorphic systems [63] and ANN accelerators [64] capable of harnessing their algorithmic capabilities. For a single update of their auxiliary learning variables (eligibility traces / errors), both RFLO and GLE incur a computational cost of $\mathcal{O}(N^2)$. Thus, for an input of duration T , all three algorithms – RFLO, GLE and BPTT (without truncation) – are on par, with a full run having a computational complexity of $\mathcal{O}(N^2T)$.

State space models (SSMs) GLE networks are linked to locally recurrent neural networks (LRNNs) (see, e.g., [65]). In recent years there has been renewed interest in similar models in the form of linear recurrent units (LRUs) [66, 67], which

combine the fast inference characteristics of LRNNs with the ease of training and stability stemming from the linearity of their recurrence. These architectures are capable of surpassing the performance of transformers in language tasks involving long sequences of tokens [68, 69].

More specifically, GLE networks are closely linked to LRUs with diagonal linear layers [70] and SSMs [71, 72], where a linear recurrence only acts locally at the level of each neuron, as realized by the leaky integration underlying the retrospective mechanism. Additionally, the inclusion of prospectivity enables the direct passthrough of input information across layers as in SSMs (see Methods Section 6.4). GLE could thus enable online training of these models, similarly to how [73] demonstrate local learning with RTRL, but with the added benefits discussed above. Since such neuron dynamics are a de-facto standard for neuromorphic architectures [63], GLE could thus open an interesting new application area for these systems, especially in light of their competitive energy footprint [74, 75].

As GLE is strongly motivated by biology, it currently only considers real-valued parameters for all connections, including the self-recurrent ones, in contrast to the complex-valued parameters in LRUs. However, an extension of GLE to complex activities appears straightforward, by directly incorporating complex time constants into prospective and retrospective operators, or, equivalently, by extending them to second order in time. With this modification, GLE would also naturally extend to the domain of complex-valued neural networks (CVNNs) [76].

4.2 Neurophysiology

Neuronal prospectivity is a core component of the GLE framework. Prospective coding in biological neurons is supported by considerable experimental and theoretical evidence [20–22, 30–32, 77] on both short and long time scales. We note that our Fourier analysis (Section 2.3 above and Methods Section 6.3) also offers a rigorous account of prospectivity in neuron models with multiple, negatively coupled variables such as the Hodgkin-Huxley mechanism or adaptation currents.

GLE further predicts functional aspects of PYR neuron morphology, as well as cortical microcircuits (CMCs) for signal and error propagation. In these CMCs, PYR cells are responsible for the transmission of both representation and error signals, as supported by ample experimental data [38–43]. Moreover, the morphological separation of the cell body into multiple distinct units, including soma, basal and apical trees, corresponds to a functional separation that allows the simultaneous representation of different pieces of information – bottom-up input, top-down errors and the resulting integrated signal – within the same cell [44]. This is also what gives synapses local access to this information, allowing the implementation of the proposed three-factor, error-correcting plasticity rule [35]. Furthermore, by representing forward activities and backward errors in separate pathways, these CMCs are capable of robust learning.

While building on many insights from previous proposals for CMCs, most notably [17, 78], we argue that our pro-

posed model features significant improvements. Our model does not require nerve cells belonging to two different classes (somatostatin-expressing (SST) interneurons and PYR cells) to closely track each others’ activity, which is more easy to reconcile with the known electrophysiology of cortical neurons. This also makes training more robust and obviates the need to copy neuronal activities when training the network for more complex tasks. Additionally, the original CMC model for error backpropagation [78] suffers from a relaxation problem, as already addressed in [17]. As it subsumes the capabilities of LE, GLE is inherently able to alleviate this problem.

Most importantly, these other CMC models are, by construction, only capable of solving purely spatial classification problems. We have shown that GLE CMCs can perform spatial and temporal tasks across a range of scales, by adapting the network parameters to the characteristic temporal and spatial timescales of the problem at hand. All of the above observations notwithstanding, it is worth noting that GLE can also apply to these alternative CMC models by implementing prospective coding in the apical dendrites of the PYR representation neurons rather than in PYR error neurons.

4.3 Open questions and future work

While the efficacy of GLE relies on correctly phase-shifting the backpropagated errors for all frequency components of the signal, their frequency-dependent gain diverges from the one required for exact gradient descent. This is not surprising, as a perfect match of gains would require the kind of perfect knowledge of the future that is available to AM/BPTT. A reasonable approximation of AM can be said to hold for $\omega\tau \lesssim 1$, but outside of this regime there is no guarantee for convergence to a good solution. Our simulations clearly demonstrate that such solutions exist and can be achieved, but it would be preferable to have a more robust mechanism for controlling gain discrepancies at high frequencies. Some straightforward and sufficient mitigation strategies might include a simple saturation of error neuron activations or the inclusion of a small synaptic time constants as proposed in [17]. However, primarily for neuromorphic realizations of GLE, we expect linear time-invariant (LTI) system theory to provide more elegant solutions, such as Bessel or all-pass (active) filters, with favorable phase-response properties and circuit-level implementations.

On a more technical note, gain amplification in prospective neurons requires particular attention in discrete-time forward-Euler simulations, where fast transients can cause a breakdown of the stability assumption for finite, fixed-size time steps on which this integration method relies. In physical, time-continuous neuronal systems, this effect is naturally mitigated by the finite time constants of all physical components, including, for example, the synapses themselves, as mentioned above.

Ideally, to ensure a close correspondence of synaptic updates between GLE and AM, errors should not disrupt representations. This can be easily achieved in the limit of weak teacher coupling $\beta \ll 1$ and/or weak somato-dendritic coupling γ . Indeed, for larger networks and more complex tasks requiring fine tuning of neuronal activities and weights, we observed an

increasing sensitivity of our networks to these parameters. To avoid these effects, we simply operated our large-scale simulations in the $\beta \rightarrow 1, \gamma \rightarrow 0$ regime. As this sensitivity also manifests as a consequence of the high-frequency gain amplification, we expect it to be correspondingly mitigated by the above-mentioned solutions.

To guarantee a perfect match between error and representation signals, pairs of PYR neurons in the two pathways ideally require an exact inversion of time constants $\tau^m \leftrightarrow \tau^r$. This relationship also needs to be maintained when time constants are learned. Similarly to the weight transport problem, we expect a certain degree of robustness to some amount of symmetry breaking [50]. However, it would be preferable to have an additional local adaptation mechanism to ensure scalability, while maintaining full compatibility with the locality constraints of physical neuronal systems. To this end, we expect that local solutions based on decay during adaptation [79], mirroring [80], and especially correlations [52] are likely to apply here as well, even more so as the matching needs to develop between active, reciprocally connected and physically proximal neurons as opposed to passive, uncoupled synapses.

GLE can be naturally extended to (more) complex neuron dynamics, as already discussed in the context of LRUs and CVNNs. Even more importantly, a GLE mechanism for (sparse) spiking dynamics as opposed to (population) rates is of eminent interest. The recently described family of solutions for backpropagation through spike times, including surrogate methods [81], exact solutions [75] and, notably, adjoint dynamics [82] suggest several starting points for deriving corresponding GLE operators.

In the presented simulations, we only applied GLE to hierarchical networks, in order to highlight its versatility in switching between spatial, temporal and spatiotemporal classification tasks without changing the underlying architecture. We expect these capabilities to extend naturally to problems of sequence generation and motor control. Moreover, the theoretical framework of GLE is architecture-agnostic, and the inclusion of lateral recurrence represents an obvious next step. We expect the approximation of AM/BPTT to be adaptable to this scenario as well, but a dedicated proof and demonstration is left for future work.

5 Conclusion

With Generalized Latent Equilibrium, we have proposed a new and flexible framework for inference and learning of complex spatio-temporal tasks in physical neuronal systems. In contrast to classical AM/BPTT, but still rivaling its performance, GLE enables efficient learning through fully local, phase-free, on-line learning in real time. Thus, GLE networks can achieve results competitive with well-known, powerful machine learning architectures such as GRUs, TCNs and convolutional neural networks (CNNs).

Our framework carries implications both for neuroscience and for the design of neuromorphic hardware. For the brain, GLE provides a rigorous theory and experimental correlates for spatio-temporal inference and learning, by leveraging an in-

terplay between retrospective and prospective coding at the neuronal level. For artificial implementations, its underlying mechanics and demonstrated capabilities may constitute powerful assets in the context of autonomous learning on low-power neuromorphic devices.

6 Methods

6.1 Detailed parameter dynamics

Error dynamics in GLE can be expressed in vector form as

$$\begin{aligned} \mathbf{e}_\ell &= \mathcal{D}_{\tau_\ell^m}^+ \left\{ \mathcal{I}_{\tau_\ell^r}^- \left\{ \mathbf{e}_\ell^{\text{inst}} \right\} \right\} \\ &= \begin{cases} \mathcal{D}_{\tau_\ell^m}^+ \left\{ \mathcal{I}_{\tau_\ell^r}^- \left\{ \boldsymbol{\varphi}'_\ell \circ \mathbf{W}_{\ell+1}^T \mathbf{e}_{\ell+1} \right\} \right\} & \text{for } \ell < L \\ \mathcal{D}_{\tau_\ell^m}^+ \left\{ \mathcal{I}_{\tau_\ell^r}^- \left\{ \boldsymbol{\varphi}'_L \circ \beta(\mathbf{r}^{\text{trg}} - \mathbf{r}_L) \right\} \right\} & \text{for } \ell = L \end{cases} \end{aligned} \quad (11)$$

With these, the parameter dynamics become

$$\dot{\mathbf{W}}_\ell \propto -\nabla_{\mathbf{W}_\ell} E = -\mathbf{e}_\ell \left(\frac{\partial \mathbf{e}_\ell}{\partial \mathbf{W}_\ell} \right)^T = \mathbf{e}_\ell \mathbf{r}_{\ell-1}^T, \quad (12)$$

$$\dot{\mathbf{b}}_\ell \propto -\nabla_{\mathbf{b}_\ell} E = -\mathbf{e}_\ell \left(\frac{\partial \mathbf{e}_\ell}{\partial \mathbf{b}_\ell} \right)^T = \mathbf{e}_\ell, \quad (13)$$

$$\dot{\tau}_\ell^m \propto -\nabla_{\tau_\ell^m} E = -\mathbf{e}_\ell \left(\frac{\partial \mathbf{e}_\ell}{\partial \tau_\ell^m} \right)^T = -\mathbf{e}_\ell \circ \dot{\mathbf{u}}_\ell, \quad (14)$$

$$\dot{\tau}_\ell^r \propto -\nabla_{\tau_\ell^r} E = -\mathbf{e}_{\ell+1} \left(\frac{\partial \mathbf{e}_{\ell+1}}{\partial \tau_\ell^r} \right)^T = \mathbf{e}_\ell^{\text{inst}} \circ \dot{\mathbf{u}}_\ell. \quad (15)$$

6.2 GLE approximates AM/BPTT in real time

In Section 2.3, we discuss how adjoint variables $\boldsymbol{\lambda}_\ell(t)$ (Eqn. 10) are approximated as GLE errors $\mathbf{e}_\ell(t)$ (Eqn. 7):

$$\begin{aligned} \boldsymbol{\lambda}_\ell(t) &= \mathcal{I}_{\tau_\ell^m}^+ \mathcal{D}_{\tau_\ell^r}^- \left\{ \boldsymbol{\varphi}'_\ell \circ \mathbf{W}_{\ell+1}^T \boldsymbol{\lambda}_{\ell+1} \right\} \\ &\approx \mathcal{D}_{\tau_\ell^m}^+ \mathcal{I}_{\tau_\ell^r}^- \left\{ \boldsymbol{\varphi}'_\ell \circ \mathbf{W}_{\ell+1}^T \mathbf{e}_{\ell+1} \right\} = \mathbf{e}_\ell(t). \end{aligned} \quad (16)$$

For a detailed derivation of the adjoint equations, we refer to Section 9 in the Supplement. In the following, we provide a detailed analysis of this relationship in Fourier (angular frequency) space.

For a linear system with input x and output y , their relationship in Fourier space is defined by the transfer function $H(\omega) = y(\omega)/x(\omega)$. In our case, these transfer functions correspond to the Fourier transforms of the prospective and retrospective operators, which we denote as $\hat{\mathcal{T}}$ and $\hat{\mathcal{D}}$. We first note the following identities:

$$\left(1 + \tau \frac{d}{dt} \right) e^{i\omega t + \psi} = (1 + i\omega\tau) e^{i\omega t + \psi}, \quad (17)$$

$$\frac{1}{\tau} \int_{-\infty}^t e^{-\frac{t-t'}{\tau}} e^{i\omega t' + \psi} dt' = \frac{1}{1 - i\omega\tau} e^{i\omega t + \psi}. \quad (18)$$

Since any signal can be written as a linear composition of such frequency components $e^{i\omega t + \psi}$, the above relationships directly translate to the Fourier transforms our operators. For a single error neuron with prospective and retrospective time constants

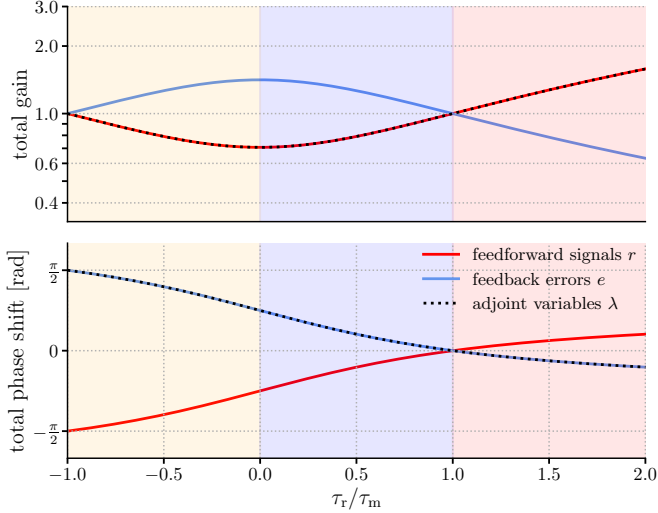


Figure 9: Total gain and phase shift of the respective components of operators in GLE and AM. Expressed as a function of τ^r/τ^m and calculated for $\omega\tau^m = 1$. Colored regions indicate different regimes of interest: negative τ^r (orange), effectively retrospective ($\tau^r < \tau^m$, blue), effectively prospective ($\tau^r > \tau^m$, red).

τ^m and τ^r , we can thus calculate

$$\begin{aligned} \widehat{\mathcal{I}}_{\tau^r}^-(\omega) &= \frac{1}{1 + i\omega\tau^r}, & \widehat{\mathcal{D}}_{\tau^m}^+(\omega) &= 1 + i\omega\tau^m, \\ \widehat{\mathcal{D}}_{\tau^r}^-(\omega) &= 1 - i\omega\tau^r, & \widehat{\mathcal{I}}_{\tau^m}^+(\omega) &= \frac{1}{1 - i\omega\tau^m}. \end{aligned} \quad (19)$$

From here, the phase shifts $\Delta\psi$ and gains G of our operators become apparent.

The phase shifts of $\widehat{\mathcal{I}}_{\tau^r}^-$ and $\widehat{\mathcal{D}}_{\tau^r}^-$ are exactly equal; the same is true for the pair $\widehat{\mathcal{D}}_{\tau^m}^+$ and $\widehat{\mathcal{I}}_{\tau^m}^+$ (see also Figs. 3 and 9):

$$\begin{aligned} \Delta\psi(\widehat{\mathcal{I}}_{\tau^r}^-) &= \Delta\psi(\widehat{\mathcal{D}}_{\tau^r}^-) = -\arctan(\omega\tau^r), \\ \Delta\psi(\widehat{\mathcal{D}}_{\tau^m}^+) &= \Delta\psi(\widehat{\mathcal{I}}_{\tau^m}^+) = \arctan(\omega\tau^m). \end{aligned} \quad (20)$$

Thus, in the combinations in which they appear in the GLE errors and adjoint equations, they induce identical phase shifts:

$$\begin{aligned} \Delta\psi\{\widehat{\mathcal{D}}_{\tau^m}^+\widehat{\mathcal{I}}_{\tau^r}^-\} &= \arctan(\omega\tau^m) - \arctan(\omega\tau^r) \\ &= \Delta\psi\{\widehat{\mathcal{I}}_{\tau^m}^+\widehat{\mathcal{D}}_{\tau^r}^-\}. \end{aligned} \quad (21)$$

The gains of the operators are given by

$$\begin{aligned} G(\widehat{\mathcal{D}}_{\tau^r}^+) &= G(\widehat{\mathcal{D}}_{\tau^r}^-) = \sqrt{1 + \omega^2(\tau^r)^2}, \\ G(\widehat{\mathcal{I}}_{\tau^r}^+) &= G(\widehat{\mathcal{I}}_{\tau^r}^-) = \frac{1}{\sqrt{1 + \omega^2(\tau^r)^2}}. \end{aligned} \quad (22)$$

This means that the GLE errors have an inverse frequency-dependent gain compared to the adjoint variables:

$$G(\widehat{\mathcal{D}}_{\tau^m}^+\widehat{\mathcal{I}}_{\tau^r}^-) = \frac{1}{G(\widehat{\mathcal{I}}_{\tau^m}^+\widehat{\mathcal{D}}_{\tau^r}^-)} = \frac{\sqrt{1 + (\omega\tau^m)^2}}{\sqrt{1 + (\omega\tau^r)^2}}. \quad (23)$$

However, the ratio of GLE and AM gains is bounded by the ratio of prospective and retrospective time constants, so that the discrepancy induced by a GLE error neuron can never exceed $(\tau^m/\tau^r)^2$.

These results extend to vectors λ_ℓ and e_ℓ , where neuronal time

constants $\{\tau^m, \tau^r\}$ are replaced by the corresponding entries in $\{\tau_\ell^m, \tau_\ell^r\}$. As the operators are linear, the above considerations apply straightforwardly to inputs with arbitrary frequency spectra, for which the operators can simply be written as convolutions over frequency space with the expressions in Eqn. 19.

Overall this shows how, by inducing phase shifts that are identical to AM for every individual frequency component of the signal, GLE errors produce parameter updates that are always in phase with the correct gradients. Even though their respective frequency-specific gains are inverted with respect to AM, their mismatch is bounded and their sign is conserved. Therefore, despite distortions at higher frequencies, GLE parameter updates remain well-aligned with their true gradients. As in GLE the propagation of (feedback) errors and (feedforward) signals is governed by the same operators, both can be easily implemented by leaky integrator neurons with prospective output dynamics.

6.3 Prospectivity through adaptation currents

In general, when neurons have additional variables that couple negatively into the membrane potential, such as certain voltage-gated ionic currents in the Hodgkin-Huxley model, or adaptation currents such as in Izhikevich [83] or AdEx [84] models, prospectivity on various time scales can naturally emerge. The intuition behind the phenomenon is as follows: an additional variable that performs a low-pass filter over either the neuronal input or the membrane potential produces a negative phase shift and attenuates high-frequency components; if subtracted from the membrane, it has the opposite effect, namely inducing a positive phase shift and increasing the gain of higher-frequency components, thus acting similarly to the prospective operator \mathcal{D}_τ^+ . Here, we demonstrate prospectivity in leaky integrator neurons with two different kinds of adaptive currents.

6.3.1 Voltage-dependent adaptive current

Consider the 2-variable neuron model

$$\begin{aligned} \tau^m \dot{u} &= -u + IR - wR, \\ \tau^w \dot{w} &= -w + \gamma_u u, \end{aligned} \quad (24)$$

where u is the membrane potential, w the adaptive current with time constant τ^w , and γ_u a coupling factor. Without loss of generality, we assume $R = 1$ for the membrane resistivity.

As in Section 6.2, we now seek the transfer function $H(\omega) = u(\omega)/I(\omega)$. To this end, we can simply rewrite the above equations using our differential operators:

$$\begin{aligned} \mathcal{D}_{\tau^m}^+ \{u\} &= I - w, \\ \mathcal{D}_{\tau^w}^+ \{w\} &= \gamma_u u. \end{aligned} \quad (25)$$

We can now apply the Fourier transform to both equations (using Eqn. 19 for the operators) and solve for $u(\omega)$, which yields the transfer function

$$H(\omega) = \frac{1 + i\omega\tau^w}{(1 + i\omega\tau^w)(1 + i\omega\tau^m) + \gamma_u}. \quad (26)$$

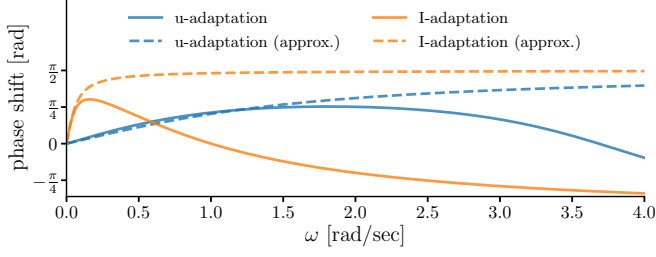


Figure 10: Adaptation enables prospectivity. The first-order analytical approximations are shown with dashed lines. Simulation parameters: $\tau^m = 1$, $\tau^w = 0.9$, $\gamma_u = 10\tau^m/\tau^w$ and $\gamma_I = (\tau^m + 0.9\tau^w)/(\tau^m + \tau^w)$.

The neuronal phase shift is given by $\Delta\psi = \arctan\left(\frac{\text{Im}(H)}{\text{Re}(H)}\right)$. Figure 10 shows a positive shift (phase advance) over a broad frequency spectrum.

We follow up with an analytical argument for low frequencies. For this model, H can be approximated by a first-order expansion in $\{\omega\tau^m, \omega\tau^w\}$:

$$H(\omega) \approx \frac{1}{1 + \gamma_u} + i\omega \frac{\gamma_u\tau^w - \tau^m}{(1 + \gamma_u)^2}, \quad (27)$$

which yields a phase shift of

$$\Delta\psi(\omega) = \arctan\left(\omega \frac{\gamma_u\tau^w - \tau^m}{1 + \gamma_u}\right). \quad (28)$$

This makes it apparent that for $\gamma_u > \frac{\tau^m}{\tau^w}$ the phase shift is positive, so the neuron is prospective.

6.3.2 Input-dependent adaptive current

With a small change, the above 2-variable model can be made directly adaptive to the input current:

$$\begin{aligned} \tau^m \dot{u} &= -u + IR - wR, \\ \tau^w \dot{w} &= -w + \gamma_I IR. \end{aligned} \quad (29)$$

The transfer function is now given by

$$H(\omega) = \frac{1 - \gamma_I + i\omega\tau^w}{(1 + i\omega\tau^w)(1 + i\omega\tau^m)},$$

which also yields a phase advance for lower input frequencies Fig. 10.

As above, we can do a first-order approximation of H in $\{\omega\tau^m, \omega\tau^w\}$:

$$H(\omega) \approx (1 - \gamma_I) + i\omega(\gamma_I\tau^w + (\gamma_I - 1)\tau^m),$$

which yields a phase-shift of

$$\Delta\psi(\omega) = \arctan\left(\omega \frac{\gamma_I\tau^w + (\gamma_I - 1)\tau^m}{1 - \gamma_I}\right). \quad (30)$$

Thus, for $\frac{\tau^m}{\tau^m + \tau^w} < \gamma_I < 1$ the membrane is prospective with respect to its input.

6.4 Relationship to SSMs

To illustrate the connection between SSMs and the GLE, we consider a single layer of the GLE model (and drop the index ℓ

and explicit time dependence (t) for brevity). First, we define a shorthand \mathbf{y} for prospective states $\mathcal{D}_{\tau^r}^+ \{\mathcal{I}_{\tau^m}^- \{\mathbf{W}\mathbf{r}\}\}$ (i.e., the neuronal output before being passed through the nonlinearity) and, as before, we use $\mathbf{u} = \mathcal{I}_{\tau^m}^- \{\mathbf{W}\mathbf{r}\}$ to denote membrane potentials. For simplicity, we have ignored the biases. We can now rewrite \mathbf{y} as

$$\begin{aligned} \mathbf{y} &= \mathcal{D}_{\tau^r}^+ \{\mathcal{I}_{\tau^m}^- \{\mathbf{W}\mathbf{r}\}\} = \mathcal{D}_{\tau^r}^+ \{\mathbf{u}\} = \mathbf{u} + \boldsymbol{\tau}^r \circ \frac{d}{dt} \mathbf{u} \\ &= (\mathbf{1} - \boldsymbol{\alpha}) \circ \mathbf{u} + \boldsymbol{\alpha} \circ \mathbf{W}\mathbf{r}, \end{aligned} \quad (31)$$

where we plugged in the integral form of the membrane potential \mathbf{u} (cf. Eqn. 1) in the last step, $\mathbf{1}$ denotes the identity vector and $\boldsymbol{\alpha} := \boldsymbol{\tau}^r/\tau^m$. We use “ \circ ” and “/” to denote element-wise multiplication and division, respectively. Then, the dynamics of membranes \mathbf{u} and prospective states \mathbf{y} are given by a system of two coupled equations

$$\begin{aligned} \dot{\mathbf{u}} &= -\frac{\mathbf{1}}{\tau^m} \circ \mathbf{u} + \frac{\mathbf{1}}{\tau^m} \circ \mathbf{W}\mathbf{r}, \\ \mathbf{y} &= (\mathbf{1} - \boldsymbol{\alpha}) \circ \mathbf{u} + \boldsymbol{\alpha} \circ \mathbf{W}\mathbf{r}. \end{aligned} \quad (32)$$

Similarly, in SSMs, inputs \mathbf{r} , latent states \mathbf{u} and observations \mathbf{y} are related by [71]

$$\begin{aligned} \dot{\mathbf{u}} &= \mathbf{A}\mathbf{u} + \mathbf{B}\mathbf{r}, \\ \mathbf{y} &= \mathbf{C}\mathbf{u} + \mathbf{D}\mathbf{r}, \end{aligned} \quad (33)$$

where \mathbf{A} , \mathbf{B} , \mathbf{C} and \mathbf{D} are matrices of appropriate dimensions. Comparing equations Eqns. 32 and 33, it is apparent that membrane potentials in GLE correspond to latent states in SSMs by setting $\mathbf{A} = -\text{diag}(\mathbf{1}/\tau^m)$ and $\mathbf{B} = \text{diag}(\mathbf{1}/\tau^m)\mathbf{W}$. Furthermore, prospective outputs in GLE correspond to observations in SSMs by setting $\mathbf{C} = \text{diag}(\mathbf{1} - \boldsymbol{\alpha})$ and $\mathbf{D} = \text{diag}(\boldsymbol{\alpha})\mathbf{W}$. Thus, GLE forward dynamics can implement a specific (diagonal) form of SSMs.

6.5 Simulation details

6.5.1 Numerical integration

We use forward Euler integration to solve the system of implicit coupled differential equations that determine the network dynamics, which simultaneously includes neuron (membrane potentials for the different compartments) and parameter (synaptic weights, neuronal biases and time constants) dynamics.

Recall the neuronal dynamics of our networks, characterized by feedforward signals at time t (we drop the (t) here for brevity)

$$\mathbf{r}_\ell = \boldsymbol{\varphi}(\mathcal{D}_{\tau_\ell^r}^+ \{\mathbf{u}_\ell\}) \quad (34)$$

$$= \boldsymbol{\varphi}\left(\mathcal{D}_{\tau_\ell^r}^+ \left\{\mathcal{I}_{\tau_\ell^m}^- \{\mathbf{W}_\ell \mathbf{r}_{\ell-1} + \mathbf{b}_\ell + \mathbf{e}_\ell\}\right\}\right) \quad (35)$$

with feedback errors

$$\mathbf{e}_\ell = \mathcal{D}_{\tau_\ell^m}^+ \{\mathbf{v}_\ell\} = \mathcal{D}_{\tau_\ell^m}^+ \left\{\mathcal{I}_{\tau_\ell^r}^- \left\{\mathbf{e}_\ell^{\text{inst}}\right\}\right\}, \quad (36)$$

where we implicitly defined the instantaneous error

$$\mathbf{e}_\ell^{\text{inst}} = \boldsymbol{\varphi}'\left(\mathcal{D}_{\tau_\ell^r}^+ \{\mathbf{u}_\ell\}\right) \circ \mathbf{W}_{\ell+1}^T \mathbf{e}_{\ell+1} - \beta \frac{\partial C}{\partial \mathcal{D}_{\tau_\ell^r}^+ \{\mathbf{u}_\ell\}}. \quad (37)$$

We first approximate the temporal derivatives of the mem-

brane potentials $\mathbf{u}_\ell(t)$ by a finite difference

$$\dot{\mathbf{u}}_\ell(t) = \left[\frac{1}{\tau_\ell^m} \circ (-\mathbf{u}_\ell + \mathbf{W}_\ell \mathbf{r}_{\ell-1} + \mathbf{e}_\ell) \right] (t) \quad (38)$$

$$\approx \frac{\mathbf{u}_\ell(t + dt) - \mathbf{u}_\ell(t)}{dt}, \quad (39)$$

where the fraction is understood to be component-wise. This equation can then be solved for the membrane potentials at the next time step:

$$\mathbf{u}_\ell(t + dt) = \left[\mathbf{u}_\ell + \frac{dt}{\tau_\ell^m} \circ (-\mathbf{u}_\ell + \mathbf{W}_\ell \mathbf{r}_{\ell-1} + \mathbf{e}_\ell) \right] (t) \quad (40)$$

Similarly, we can approximate the derivative of the error neuron potentials $\mathbf{v}_\ell(t)$ and solve for the potentials at the next time step:

$$\mathbf{v}_\ell(t + dt) = \left[\mathbf{v}_\ell + \frac{dt}{\tau_\ell^r} \circ (-\mathbf{v}_\ell + \mathbf{e}_\ell^{\text{inst}}) \right] (t) \quad (41)$$

The learning dynamics (Eqns. 12 to 15) are discretized accordingly. For example, the update of the synaptic weights \mathbf{W}_ℓ is given by

$$\mathbf{W}_\ell(t + dt) = \left[\mathbf{W}_\ell + \underbrace{\frac{dt}{\tau_\ell^W}}_{\eta_\ell^W} \circ \mathbf{e}_\ell \mathbf{r}_{\ell-1}^\top \right] (t). \quad (42)$$

This system of equations is summarized in Algorithm 1.

Algorithm 1 Forward Euler simulation of GLE network

```

initialize network parameters  $\theta = \{\mathbf{W}, \mathbf{b}, \tau^m, \tau^r\}$ 
initialize network states at  $t = 0$ :  $\mathbf{u}(0), \mathbf{v}(0), \mathbf{r}(0), \mathbf{e}(0)$ 
for time step  $t$  in  $[0, T]$  with step size  $dt$  do
  for layer  $\ell$  from 1 to  $L$  do
    if  $\ell = L$  then
      calculate instantaneous target error:
       $\mathbf{e}_L^{\text{inst}}(t + dt) \leftarrow \beta \varphi'_L(t) \circ (\mathbf{r}^{\text{trg}}(t) - \mathbf{r}_L(t))$ 
    else
      propagate feedback error signals:
       $\mathbf{e}_\ell^{\text{inst}}(t + dt) \leftarrow \varphi'_\ell(t) \circ \mathbf{W}_{\ell+1}^\top(t) \mathbf{e}_{\ell+1}(t)$ 
    end if
    sum input currents:
     $\mathbf{I}_\ell(t) = \mathbf{W}_\ell(t) \mathbf{r}_{\ell-1}(t) + \mathbf{b}_\ell(t) + \gamma \mathbf{e}_\ell(t)$ 
    approximate membrane potential derivatives:
     $\Delta \mathbf{u}_\ell(t) \leftarrow (\tau_\ell^m(t))^{-1} \circ (-\mathbf{u}_\ell(t) + \mathbf{I}_\ell(t))$ 
    update membrane potentials:
     $\mathbf{u}_\ell(t + dt) \leftarrow \mathbf{u}_\ell(t) + dt \Delta \mathbf{u}_\ell(t)$ 
    approximate error potential derivatives:
     $\Delta \mathbf{v}_\ell(t) \leftarrow (\tau_\ell^r(t))^{-1} \circ (-\mathbf{v}_\ell(t) + \mathbf{e}_\ell^{\text{inst}}(t))$ 
    update error potentials:
     $\mathbf{v}_\ell(t + dt) \leftarrow \mathbf{v}_\ell(t) + dt \Delta \mathbf{v}_\ell(t)$ 
    update prospective error potentials:
     $\mathbf{e}_\ell(t + dt) \leftarrow \mathbf{v}_\ell(t) + \tau_\ell^m(t) \circ \Delta \mathbf{v}_\ell(t)$ 
    calculate prospective outputs:
     $\mathbf{r}_\ell(t + dt) \leftarrow \varphi(\mathbf{u}_\ell(t) + \tau_\ell^r(t) \circ \Delta \mathbf{u}_\ell(t))$ 
    update synaptic weights:
     $\mathbf{W}_\ell(t + dt) \leftarrow \mathbf{W}_\ell(t) + \eta_W \mathbf{e}_\ell(t) \mathbf{r}_{\ell-1}^\top(t)$ 
    update biases:
     $\mathbf{b}_\ell(t + dt) \leftarrow \mathbf{b}_\ell(t) + \eta_b \mathbf{e}_\ell(t)$ 
    update membrane time constants:
     $\tau_\ell^m(t + dt) \leftarrow \tau_\ell^m(t) - \eta_\tau \mathbf{e}_\ell(t) \circ \Delta \mathbf{u}_\ell(t)$ 
    update prospective time constants:
     $\tau_\ell^r(t + dt) \leftarrow \tau_\ell^r(t) + \eta_\tau \mathbf{e}_\ell^{\text{inst}}(t) \circ \Delta \mathbf{v}_\ell(t)$ 
  end for
end for

```

Note that in addition to the nudging strength β that scales the target error, we introduce another parameter γ to scale

the coupling between the apical dendritic and somatic compartments, thus controlling the feedback of the error signals \mathbf{e} into the somatic potentials \mathbf{u} .

6.5.2 General simulation details for the GLE networks

Our networks are implemented in Python using the PyTorch library. All vector quantities with a layer index ℓ are implemented as PyTorch tensors. Neuronal activation functions are hyperbolic tangents.

For the cost function C , we either use a mean-squared error (MSE)

$$C = \frac{1}{2} \sum_{i \in L} (r_i^{\text{trg}} - r_i)^2 \quad (43)$$

with outputs

$$r_i = \varphi \left(\mathcal{D}_{\tau_i^+} \{u_i\} \right) \quad (44)$$

or a cross-entropy (CE) loss

$$C = - \sum_{i \in L} r_i^{\text{trg}} \log(r_i) \quad (45)$$

with softmax outputs

$$r_i = \exp \left(\mathcal{D}_{\tau_i^+} \{u_i\} \right) / \sum_j \exp \left(\mathcal{D}_{\tau_j^+} \{u_j\} \right) \quad (46)$$

depending on the task. In both cases, the \mathbf{r}^{trg} is either a target rate or a one-hot vector encoding the target class.

In the two teacher-student setups, the target output rate is produced by a teacher network with the same architecture as the student, but with fixed weights and time constants. Student networks trained with different algorithms are initialized with identical but randomized parameters. The outputs of teacher and student are compared via the MSE loss.

Time units are fixed but arbitrary, so we can treat time as unit-free in the following.

6.5.3 GLE chain (Section 3.1 and Fig. 5)

The input signal is a smoothed square wave of amplitude 1 and period $T = 4$, with a simulation time step of $dt = 0.01$. Batches of 100 samples are generated by shifting the input randomly in time by values between 0 and $T/2$. Teacher weights and time constants are $w_0 = 1$, $w_1 = 2$, $\tau_0^m = 1$, $\tau_2^m = 2$, $\tau_0^r = \tau_1^r = 0.1$. The two student networks trained with GLE and instantaneous BP use a learning rate of 0.0001 and a nudging strength of $\beta = 0.01$. The three student networks trained with truncated BPTT and truncation windows of 1, 2 and 4 use learning rates of 0.01, 0.02, and 0.04, respectively. All networks use the Adam optimizer [85] with default parameters for momentum and decay rates for faster convergence.

6.5.4 Small networks (Section 3.2 and Fig. 6)

The input signal is a composition of three sine signals with frequencies $\omega^1 = 0.49$, $\omega^2 = 1.07$, and $\omega^3 = 1.98$. To isolate the effect of backpropagated errors over multiple layers, only the bottom weights are initialized randomly and then learned. The

Table 1: Neuron, network and training parameters used to produce the results shown in Fig. 8.

Symbol	Parameter name	MNIST1D GLE (15k)	MNIST1D GLE (42k)	MNIST1D LagNet + LE	GSC GLE
Dynamic parameters in arbitrary units					
dt	simulation time step	0.2	0.2	0.2	0.05
T	sample duration	$72 = 360 dt$	$72 = 360 dt$	$72 = 360 dt$	$41\text{ms}/\text{mfcc} = 820 dt$
τ^m	membrane time constants	$[1.2, 1.2, 0.6]^1$	$[1.2, 0.6, 0.2]^1$	1.0	$[2.4, 0.6, 1.2, 1.8, 2.4]^1$
τ^r	prospective time constants	$[0.6, 0.2, 0.2]^1$	$[0.6, 0.2, 0.2]^1$	1.0	$[2.4, 0.1, 0.1, 0.1, 0.1]^1$
Network parameters					
φ_ℓ	activation	tanh	tanh	tanh	tanh
φ_L	output activation	softmax	softmax	softmax	softmax
\mathcal{C}	cost	cross-entropy	cross-entropy	cross-entropy	cross-entropy
	architecture	GLE FC	GLE FC	LagNet ² + LE-MLP	GLE FC
	number of hidden layers	6	6	2	3
	input size	1	1	10	32
	hidden layer size	$17 + 18 + 18$	$30 + 30 + 30$	$60 + 60$	$150 + 150 + 150 + 150 + 150$
	output layer size	10	10	10	12
β	nudging strength	1.0	1.0	1.0	1.0
γ	apical-somatic coupling	0.0	0.0	0.0	0.0
$\eta_{W,b}$	learning rate	0.01	0.005	0.005	0.005
$W_{\text{init}}, b_{\text{init}}$	initial weights & biases	$\mathcal{U}(-\sqrt{k}, \sqrt{k})$ with $k = 1/\text{fan-in}^3$			
	optimizer	Adam [85] with PyTorch's default parameters			
	lr scheduler	ReduceOnPlateau		ReduceOnPlateau	
	lr scheduler params	$\gamma = 0.5, \text{patience}=2$		$\gamma = 0.9, \text{patience}=3$	
Training parameters					
	batch size	100	100	100	256
	# training epochs	150	150	150	200
	# train samples	4000	4000	4000	36923
	# validation samples	1000	1000	1000	4445
	# seeds	10	10	10	10

¹ Time constants of the three neuron populations in each hidden layer.

² The LagNet has a single input that projects onto four hidden layers with ten neurons each. The layers are connected with identity weight matrices and not learned. Each hidden layer uses linearly distributed membrane time constants between $\tau^m = [dt = 0.2, \dots, 1.8]$ and equal $\tau^r = dt = 0.2$. This allows for a mapping of the temporal sequence to spatially distributed representations. The output of the last hidden layer is fed into the plastic (G)LE network.

loss depicted in Fig. 6f is filtered with a rectangular window of width 1. The AM (see also Algorithm 2 in the Supplement) uses a truncation window of duration 3. Learning rates are $\eta_{\text{GLE}} = 2 \times 10^{-2}$ and $\eta_{\text{AM}} = 7 \times 10^{-2}$. We use a teacher nudging strength of $\beta = 1$, and a somato-dendritic coupling of $\gamma = 10^{-3}$. The frequency resolution in Fig. 6c,d is given by $\frac{2\pi}{n dt}$, where n is the window length over which the frequency spectrum is calculated. To calculate the frequency spectrum of the signals before and during the early learning phase, the network is simulated for $n = 8000$ steps with fixed weights (yielding a frequency resolution of ≈ 0.078).

6.5.5 MNIST-1D (Section 3.3.1/3.3.3 and Fig. 8d/f)

The GLE networks in Fig. 8d use a layered architecture with a single input neuron in the first layer, six fully connected hidden layers and an output layer with ten neurons. Each hidden layer has three different populations of neurons, each with different time constants τ^m and τ^r . The (G)LE networks in Fig. 8f use a custom, non-plastic LagNet of purely retrospective neurons ($\tau^r = 0$) with different membrane time constants τ^m that allow for an approximate, partial mapping of the temporal sequence to the neuronal space. Detailed parameters for the different GLE networks are given in Table 1.

The original publication of the dataset [54] uses a downsampled version of the sequences to 40 time steps (baseline results with index 0 in Fig. 8f). For a more continuous input, we interpolate the original sequences of length 72 to 360 time steps. To ensure a fair comparison, we also retrain the baseline architectures on these higher-resolution sequences (Fig. 8d). An

overview over the different reference models, their size and final performance on the MNIST-1D dataset is shown in Table 2 in the Supplement.

6.5.6 Google Speech Commands

The GLE networks use a layered architecture with 32 input neurons in the first layer, 3 fully-connected hidden layers and an output layer with twelve neurons. Each hidden layer has five different populations of neurons, each with different time constants τ^m and τ^r . Detailed parameters for the different GLE networks are given in the last column of Table 1.

To provide a fair comparison, the dataset (v2.12) and data augmentation process from [86] is used to train and test all models. For a more continuous input, the original sequences are interpolated, increasing the number of time steps by a factor of 20. The train/validation/test set split ratio is 80:10:10. The training data is augmented with background noise and random time shifts of up to 100 ms. The length and stride of the Fourier window, the number of frequency bins and the type of Mel frequency representation is optimized for each method independently; all parameters are given in Table 3 in the Supplement.

7 Acknowledgements

We thank Simon Brandt for sharing his expertise on prospectivity in mechanistic neuron models and Walter Senn for many stimulating discussions about various aspects of dendritic computation, energy-based models, error-correcting plasticity

and bio-plausible credit assignment. We gratefully acknowledge funding from the European Union under grant agreement #945539 (Human Brain Project, SGA3), the Volkswagen Foundation under the call “NEXT – Neuromorphic Computing” for partially funding KM’s contribution and ESKAS for funding IJ’s contribution under a Swiss Government Excellence Scholarship. We would like to express particular gratitude for the ongoing support from the Mandred Stärk Foundation. Our work has greatly benefitted from access to the Fenix Infrastructure resources, which are partially funded by the European Union’s Horizon 2020 research and innovation programme through the ICEI project under the grant agreement No. 800858. Furthermore, we thank Marcel Affolter, Reinhard Dietrich and the Insel Data Science Center for the usage and outstanding support of their Research HPC Cluster.

8 Author contributions

BE and PH share first authorship of the manuscript. MAP, PH and BE conceived the core ideas and designed the project. BE and MAP initiated the project and produced the first results. PH, BE, IJ, JJ and LK developed the code and performed the simulations. PH, KM, FB, IJ and MAP developed the proof of correspondence between GLE and AM. All authors contributed to the development of the theory and simulations. All authors contributed to writing the manuscript. Corresponding authors: paul.haider@unibe.ch and mihai.petrovici@unibe.ch.

References

1. Baydin, A. G., Pearlmutter, B. A., Radul, A. A. & Siskind, J. M. Automatic Differentiation in Machine Learning: A Survey. *Journal of Machine Learning Research* **18**, 1–43. ISSN: 1533-7928 (2018).
2. Pearlmutter, B. Gradient Calculations for Dynamic Recurrent Neural Networks: A Survey. *IEEE Transactions on Neural Networks* **6**, 1212–1228. ISSN: 1941-0093 (Sept. 1995).
3. Linnainmaa, S. Taylor Expansion of the Accumulated Rounding Error. *BIT Numerical Mathematics* **16**, 146–160. ISSN: 1572-9125 (June 1976).
4. Werbos, P. J. Applications of Advances in Nonlinear Sensitivity Analysis. *Proc. IFIP* (eds Drenick, R & Kozin, F) (1982).
5. Rumelhart, D. E., Hinton, G. E. & Williams, R. J. Learning Representations by Back-Propagating Errors. *Nature* **323**, 533–536. ISSN: 1476-4687 (Oct. 1986).
6. Pineda, F. J. Generalization of Back-Propagation to Recurrent Neural Networks. *Physical Review Letters* **59**, 2229–2232 (Nov. 1987).
7. Werbos, P. Backpropagation through Time: What It Does and How to Do It. *Proceedings of the IEEE* **78**, 1550–1560. ISSN: 1558-2256 (Oct. 1990).
8. Kelley, H. J. in, 205–254 (Elsevier, 1962).
9. Todorov, E. in (eds Doya, K., Ishii, S., Pouget, A. & Rao, R. P.) 12: 1–28 (MIT Press, 2006).
10. Chachuat, B. Nonlinear and Dynamic Optimization: From Theory to Practice. *Lecture notes, EPFL*, 1–187 (2007).
11. Sutton, R. *Reinforcement learning* 2nd (MIT Press, 2018).
12. Lillicrap, T. P. & Santoro, A. Backpropagation through Time and the Brain. *Current Opinion in Neurobiology. Machine Learning, Big Data, and Neuroscience* **55**, 82–89. ISSN: 0959-4388 (Apr. 2019).
13. Sussillo, D. & Abbott, L. F. Generating coherent patterns of activity from chaotic neural networks. *Neuron* **63**, 544–557 (2009).
14. Gilra, A. & Gerstner, W. Predicting Non-Linear Dynamics by Stable Local Learning in a Recurrent Spiking Neural Network. *eLife* **6** (ed Latham, P.) e28295. ISSN: 2050-084X (Nov. 2017).
15. Williams, R. J. & Zipser, D. A learning algorithm for continually running fully recurrent neural networks. *Neural Computation* **1**, 270–280 (1989).
16. Marschall, O., Cho, K. & Savin, C. A Unified Framework of Online Learning Algorithms for Training Recurrent Neural Networks. *Journal of Machine Learning Research* **21**, 1–34. ISSN: 1533-7928 (2020).
17. Haider, P. et al. Latent Equilibrium: A Unified Learning Theory for Arbitrarily Fast Computation with Arbitrarily Slow Neurons. *Advances in Neural Information Processing Systems* **34**, 17839–17851 (2021).
18. Hodgkin, A. L. & Huxley, A. F. A Quantitative Description of Membrane Current and Its Application to Conduction and Excitation in Nerve. *The Journal of Physiology* **117**, 500–544. ISSN: 0022-3751 (Aug. 1952).
19. Köndgen, H. et al. The Dynamical Response Properties of Neocortical Neurons to Temporally Modulated Noisy Inputs In Vitro. *Cerebral Cortex* **18**, 2086–2097. ISSN: 1047-3211 (Sept. 2008).
20. Plesser, H. E. & Gerstner, W. Escape Rate Models for Noisy Integrate-and-Free Neurons. *Neurocomputing* **32–33**, 219–224. ISSN: 0925-2312 (June 2000).
21. Pozzorini, C., Naud, R., Mensi, S. & Gerstner, W. Temporal whitening by power-law adaptation in neocortical neurons. *Nature Neuroscience* **16**, 942–948 (2013).
22. Brandt, S., Petrovici, M. A., Senn, W., Wilmes, K. A. & Benitez, F. Prospective and Retrospective Coding in Cortical Neurons. eprint: 2405.14810 (q-bio) (May 2024).
23. Aamir, S. A. et al. A mixed-signal structured AdEx neuron for accelerated neuromorphic cores. *IEEE Transactions on Biomedical Circuits and Systems* **12**, 1027–1037 (2018).
24. Rubino, A., Payvand, M. & Indiveri, G. Ultra-low power silicon neuron circuit for extreme-edge neuromorphic intelligence. *26th IEEE International Conference on Electronics, Circuits and Systems (ICECS)*, 458–461 (2019).

25. Shaban, A., Bezugam, S. S. & Suri, M. An adaptive threshold neuron for recurrent spiking neural networks with nanodevice hardware implementation. *Nature Communications* **12**, 4234 (2021).
26. Billaudelle, S., Weis, J., Dauer, P. & Schemmel, J. An accurate and flexible analog emulation of AdEx neuron dynamics in silicon. *2022 29th IEEE International Conference on Electronics, Circuits and Systems (ICECS)*, 1–4 (2022).
27. Hopfield, J. J. Neural Networks and Physical Systems with Emergent Collective Computational Abilities. *Proceedings of the National Academy of Sciences* **79**, 2554–2558 (Apr. 1982).
28. Ackley, D. H., Hinton, G. E. & Sejnowski, T. J. A Learning Algorithm for Boltzmann Machines. *Cognitive Science* **9**, 147–169. ISSN: 0364-0213, 1551-6709 (Jan. 1985).
29. Scellier, B. & Bengio, Y. Equilibrium Propagation: Bridging the Gap Between Energy-Based Models and Backpropagation. arXiv: 1602.05179 [cs] (Mar. 2017).
30. Mainen, Z. F., Joerges, J., Huguenard, J. R. & Sejnowski, T. J. A model of spike initiation in neocortical pyramidal neurons. en. *Neuron* **15**, 1427–1439. ISSN: 08966273 (Dec. 1995).
31. Gerstner, W., Kistler, W. M., Naud, R. & Paninski, L. *Neuronal Dynamics: From Single Neurons to Networks and Models of Cognition* 1st ed. ISBN: 9781107060838 9781107635197 9781107447615 (Cambridge University Press, July 2014).
32. Traub, R. D. & Miles, R. *Neuronal Networks of the Hippocampus* 1st ed. ISBN: 9780521364812 9780521063319 97805211895401 (Cambridge University Press, May 1991).
33. Linaro, D., Biró, I. & Giugliano, M. Dynamical response properties of neocortical neurons to conductance-driven time-varying inputs. *European Journal of Neuroscience* **47**, 17–32 (2018).
34. Richards, B. A. et al. A deep learning framework for neuroscience. *Nature Neuroscience* **22**, 1761–1770 (2019).
35. Urbanczik, R. & Senn, W. Learning by the dendritic prediction of somatic spiking. *Neuron* **81**, 521–528 (2014).
36. Markov, N. T. et al. Anatomy of hierarchy: feedforward and feedback pathways in macaque visual cortex. *Journal of Comparative Neurology* **522**, 225–259 (2014).
37. Shai, A. S., Anastassiou, C. A., Larkum, M. E. & Koch, C. Physiology of layer 5 pyramidal neurons in mouse primary visual cortex: coincidence detection through bursting. *PLoS Computational Biology* **11**, e1004090 (2015).
38. Zmarz, P. & Keller, G. B. Mismatch receptive fields in mouse visual cortex. *Neuron* **92**, 766–772 (2016).
39. Fiser, A. et al. Experience-dependent spatial expectations in mouse visual cortex. *Nature Neuroscience* **19**, 1658–1664 (2016).
40. Attinger, A., Wang, B. & Keller, G. B. Visuomotor coupling shapes the functional development of mouse visual cortex. *Cell* **169**, 1291–1302 (2017).
41. Keller, G. B. & Mrsic-Flogel, T. D. Predictive Processing: A Canonical Cortical Computation. *Neuron* **100**, 424–435. ISSN: 08966273 (Oct. 2018).
42. Ayaz, A. et al. Layer-specific integration of locomotion and sensory information in mouse barrel cortex. *Nature Communications* **10**, 2585 (2019).
43. Gillon, C. J. et al. Responses to pattern-violating visual stimuli evolve differently over days in somata and distal apical dendrites. *Journal of Neuroscience* **44** (2024).
44. Francioni, V., Tang, V. D., Brown, N. J., Toloza, E. H. & Harnett, M. Vectorized Instructive Signals in Cortical Dendrites during a Brain-Computer Interface Task. bioRxiv: 2023.11.03.565534 (2023).
45. Wilson, N. R., Runyan, C. A., Wang, F. L. & Sur, M. Division and subtraction by distinct cortical inhibitory networks in vivo. *Nature* **488**, 343–348 (2012).
46. Seybold, B. A., Phillips, E. A., Schreiner, C. E. & Hasenstaub, A. R. Inhibitory actions unified by network integration. *Neuron* **87**, 1181–1192 (2015).
47. Lee, S., Kruglikov, I., Huang, Z. J., Fishell, G. & Rudy, B. A disinhibitory circuit mediates motor integration in the somatosensory cortex. *Nature Neuroscience* **16**, 1662–1670 (2013).
48. Dorsett, C., Philpot, B. D., Smith, S. L. & Smith, I. T. The impact of SST and PV interneurons on nonlinear synaptic integration in the neocortex. *eNeuro* **8** (2021).
49. Petrovici, M. A. *Form versus function: theory and models for neuronal substrates* (Springer, 2016).
50. Lillicrap, T. P., Cownden, D., Tweed, D. B. & Akerman, C. J. Random synaptic feedback weights support error backpropagation for deep learning. *Nature communications* **7**, 13276 (2016).
51. Meulemans, A., Farinha, M. T., Cervera, M. R., Sacramento, J. & Grewe, B. F. *Minimizing control for credit assignment with strong feedback* PMLR, 2022.
52. Max, K. et al. Learning efficient backprojections across cortical hierarchies in real time. *Nature Machine Intelligence* **6**, 619–630. ISSN: 2522-5839 (2024).
53. Bai, S., Kolter, J. Z. & Koltun, V. An Empirical Evaluation of Generic Convolutional and Recurrent Networks for Sequence Modeling. arXiv: 1803.01271 [cs.LG] (2018).
54. Greydanus, S. Scaling down Deep Learning. eprint: 2011.14439 (cs, stat) (2020).
55. Cho, K. et al. Learning Phrase Representations using RNN Encoder-Decoder for Statistical Machine Translation. arXiv: 1406.1078 [cs.CL] (2014).
56. Warden, P. Speech Commands: A Dataset for Limited-Vocabulary Speech Recognition. arXiv: 1804.03209 [cs.CL] (2018).
57. Hochreiter, S. & Schmidhuber, J. Long short-term memory. *Neural Computation* **9**, 1735–1780 (1997).
58. LeCun, Y. et al. Backpropagation applied to handwritten zip code recognition. *Neural Computation* **1**, 541–551 (1989).

59. Krizhevsky, A., Hinton, G., et al. Learning multiple layers of features from tiny images (2009).
60. Senn, W. et al. A Neuronal Least-Action Principle for Real-Time Learning in Cortical Circuits. *eLife* **12** (2023).
61. Williams, R. J. & Zipser, D. in, 433–486 (Lawrence Erlbaum Associates, Inc, Hillsdale, NJ, US, 1995). ISBN: 978-0-8058-1258-9 978-0-8058-1259-6.
62. Murray, J. M. Local Online Learning in Recurrent Networks with Random Feedback. *eLife* **8**, e43299. ISSN: 2050-084X (May 2019).
63. Schuman, C. D. et al. A survey of neuromorphic computing and neural networks in hardware. arXiv: 1705.06963 (2017).
64. Deng, L., Li, G., Han, S., Shi, L. & Xie, Y. Model compression and hardware acceleration for neural networks: A comprehensive survey. *Proceedings of the IEEE* **108**, 485–532 (2020).
65. Campolucci, P., Uncini, A. & Piazza, F. Causal Back Propagation through Time for Locally Recurrent Neural Networks. *1996 IEEE International Symposium on Circuits and Systems. Circuits and Systems Connecting the World. ISCAS 96* **3**, 531–534 vol.3 (May 1996).
66. Orvieto, A. et al. Resurrecting Recurrent Neural Networks for Long Sequences. *Proceedings of the 40th International Conference on Machine Learning*, 26670–26698. ISSN: 2640-3498 (July 2023).
67. Orvieto, A., De, S., Gulcehre, C., Pascanu, R. & Smith, S. L. Universality of Linear Recurrences Followed by Non-linear Projections: Finite-Width Guarantees and Benefits of Complex Eigenvalues. eprint: 2307.11888 (cs) (Mar. 2024).
68. Gu, A. & Dao, T. Mamba: Linear-Time Sequence Modeling with Selective State Spaces. eprint: 2312.00752 (cs) (Dec. 2023).
69. De, S. et al. Griffin: Mixing Gated Linear Recurrences with Local Attention for Efficient Language Models. eprint: 2402.19427 (cs) (Feb. 2024).
70. Gupta, A., Gu, A. & Berant, J. Diagonal state spaces are as effective as structured state spaces. *Advances in Neural Information Processing Systems* **35**, 22982–22994 (2022).
71. Gu, A. et al. Combining recurrent, convolutional, and continuous-time models with linear state space layers. *Advances in Neural Information Processing Systems* **34**, 572–585 (2021).
72. Gu, A., Goel, K. & Ré, C. Efficiently modeling long sequences with structured state spaces. arXiv: 2111.00396 (2021).
73. Zucchet, N., Meier, R., Schug, S., Mujika, A. & Sacramento, J. Online Learning of Long-Range Dependencies. eprint: 2305.15947 (cs) (2023).
74. Wunderlich, T. et al. Demonstrating advantages of neuromorphic computation: a pilot study. *Frontiers in Neuroscience* **13**, 260 (2019).
75. Göltz, J. et al. Fast and Energy-Efficient Neuromorphic Deep Learning with First-Spike Times. *Nature Machine Intelligence* **3**, 823–835. ISSN: 2522-5839 (Sept. 2021).
76. Lee, C., Hasegawa, H. & Gao, S. Complex-valued neural networks: A comprehensive survey. *IEEE/CAA Journal of Automatica Sinica* **9**, 1406–1426 (2022).
77. Brette, R. et al. Simulation of networks of spiking neurons: A review of tools and strategies. en. *Journal of Computational Neuroscience* **23**, 349–398. ISSN: 1573-6873 (Dec. 2007).
78. Sacramento, J., Ponte Costa, R., Bengio, Y. & Senn, W. Dendritic Cortical Microcircuits Approximate the Backpropagation Algorithm. *Advances in Neural Information Processing Systems* **31** (2018).
79. Kolen, J. F. & Pollack, J. B. Backpropagation without weight transport. *Proceedings of 1994 IEEE International Conference on Neural Networks (ICNN'94)* **3**, 1375–1380 (1994).
80. Akrouf, M., Wilson, C., Humphreys, P., Lillicrap, T. & Tweed, D. B. Deep learning without weight transport. *Advances in Neural Information Processing Systems* **32** (2019).
81. Cramer, B. et al. Surrogate gradients for analog neuromorphic computing. *Proceedings of the National Academy of Sciences* **119** (2022).
82. Wunderlich, T. C. & Pehle, C. Event-based backpropagation can compute exact gradients for spiking neural networks. *Scientific Reports* **11**, 12829 (2021).
83. Izhikevich, E. M. Simple model of spiking neurons. *IEEE Transactions on Neural Networks* **14**, 1569–1572 (2003).
84. Brette, R. & Gerstner, W. Adaptive exponential integrate-and-fire model as an effective description of neuronal activity. *Journal of Neurophysiology* **94**, 3637–3642 (2005).
85. Kingma, D. P. & Ba, J. Adam: A method for stochastic optimization. arXiv: 1412.6980 (2014).
86. Zhang, Y., Suda, N., Lai, L. & Chandra, V. Hello Edge: Keyword Spotting on Microcontrollers. arXiv: 1711.07128 [cs.SD] (2018).

Supplementary Information

9 Adjoint equations and parameter updates for the feedforward pathway in GLE networks

The general problem we aim to solve is to minimize some cost $\mathcal{C}(\mathbf{u}, \dot{\mathbf{u}}, \boldsymbol{\theta})$ through adaptation of the parameters $\boldsymbol{\theta} \in \{\mathbf{W}, \mathbf{b}, \boldsymbol{\tau}^m, \boldsymbol{\tau}^r\}$ of a dynamical system with presynaptic inputs \mathbf{r}_{in} , which is constrained by the dynamics of state variables \mathbf{u} . The dynamics are described by a system of ordinary differential equations (ODEs) in implicit form

$$\mathbf{h}(\mathbf{u}, \dot{\mathbf{u}}, \boldsymbol{\theta}, t) = \boldsymbol{\tau}^m \dot{\mathbf{u}} + \mathbf{u} - \mathbf{W} \mathbf{r}_{\text{in}} - \mathbf{b} = 0. \quad (47)$$

Note that this is a special case of the GLE dynamics, where the error term \mathbf{e} is zero and the solution is given by

$$\mathbf{u}(t) = \mathcal{I}_{\boldsymbol{\tau}^m} \{\mathbf{W} \mathbf{r}_{\text{in}} + \mathbf{b}\}. \quad (48)$$

We define the cost functional \mathcal{C} as the integral of the instantaneous cost C over some time interval $[0, T]$

$$\mathcal{C}(\mathbf{u}, \dot{\mathbf{u}}, \boldsymbol{\theta}) = \int_0^T C(t, \mathbf{u}, \dot{\mathbf{u}}, \boldsymbol{\theta}) dt, \quad (49)$$

where the instantaneous cost can be defined as the mean-squared error between the target rate \mathbf{r}^{trg} and the actual rate \mathbf{r} at time t of some subset \mathcal{O} of all the neurons in the network \mathcal{N} , $C(t, \mathbf{u}, \dot{\mathbf{u}}, \boldsymbol{\theta}) = \frac{1}{2} \sum_{o \in \mathcal{O}} \|\mathbf{r}^{\text{trg}}(t) - \mathbf{r}(t, \mathbf{u}_o, \dot{\mathbf{u}}_o)\|^2$. In practice, \mathcal{C} could represent the integrated cost over a data sample or a window of a continuous input stream of length T .

In order to solve the constrained optimization problem with AM, we first introduce the Lagrangian

$$\mathcal{L} \equiv \int_0^T C(t, \mathbf{u}(t), \dot{\mathbf{u}}(t), \boldsymbol{\theta}) + \boldsymbol{\lambda}^T(t) \mathbf{h}(t, \mathbf{u}(t), \dot{\mathbf{u}}(t), \boldsymbol{\theta}) dt, \quad (50)$$

where $\boldsymbol{\lambda}(t)$ acts a Lagrangian multiplier. The gradient of the Lagrangian \mathcal{L} w.r.t. the parameters $\boldsymbol{\theta}$ reads (suppressing the explicit time-dependence from here on)

$$\frac{d\mathcal{L}}{d\boldsymbol{\theta}} = \int_0^T \left\{ \left[\frac{\partial C}{\partial \boldsymbol{\theta}} + \frac{\partial C}{\partial \mathbf{u}} \frac{d\mathbf{u}}{d\boldsymbol{\theta}} + \frac{\partial C}{\partial \dot{\mathbf{u}}} \frac{d\dot{\mathbf{u}}}{d\boldsymbol{\theta}} \right] + \underbrace{\frac{d\boldsymbol{\lambda}^T}{d\boldsymbol{\theta}}}_{=0} \mathbf{h} + \boldsymbol{\lambda}^T \left(\frac{\partial \mathbf{h}}{\partial \boldsymbol{\theta}} + \frac{\partial \mathbf{h}}{\partial \mathbf{u}} \frac{d\mathbf{u}}{d\boldsymbol{\theta}} + \frac{\partial \mathbf{h}}{\partial \dot{\mathbf{u}}} \frac{d\dot{\mathbf{u}}}{d\boldsymbol{\theta}} \right) \right\} dt. \quad (51)$$

The term proportional to \mathbf{h} vanishes, as $\mathbf{h} = 0$ is satisfied at all times t . Most of the remaining terms can be simplified upon substituting one of the specific parameters $\boldsymbol{\theta}$. In the following we derive the parameter updates for the synaptic weights \mathbf{W} . We do so first for a single vector of output neurons (i.e., neurons receiving external targets; this corresponds to the output layer in a hierarchical network) and then extend the derivation to hidden layers.

9.1 Output neurons

After integrating by parts the terms including $d\dot{\mathbf{u}}/d\mathbf{W}$, we can rewrite the gradient as

$$\frac{d\mathcal{L}}{d\mathbf{W}} = \int_0^T \left\{ \frac{\partial C}{\partial \mathbf{W}} + \boldsymbol{\lambda}^T \frac{\partial \mathbf{h}}{\partial \mathbf{W}} + \left[\frac{\partial C}{\partial \mathbf{u}} - \frac{d}{dt} \frac{\partial C}{\partial \dot{\mathbf{u}}} + \boldsymbol{\lambda}^T \frac{\partial \mathbf{h}}{\partial \mathbf{u}} - \dot{\boldsymbol{\lambda}}^T \frac{\partial \mathbf{h}}{\partial \dot{\mathbf{u}}} - \boldsymbol{\lambda}^T \frac{d}{dt} \frac{\partial \mathbf{h}}{\partial \dot{\mathbf{u}}} \right] \frac{d\mathbf{u}}{d\mathbf{W}} \right\} dt + \left[\left(\boldsymbol{\lambda}^T \frac{\partial \mathbf{h}}{\partial \dot{\mathbf{u}}} + \frac{\partial C}{\partial \dot{\mathbf{u}}} \right) \frac{\partial \mathbf{u}}{\partial \mathbf{W}} \right]_0^T. \quad (52)$$

To set boundary terms of the dynamical system at $t = T$ to zero in Eqn. 52, we choose

$$\boldsymbol{\lambda}(T) = - \left(\frac{\partial \mathbf{h}}{\partial \dot{\mathbf{u}}} \right)^{-1} \frac{\partial C}{\partial \dot{\mathbf{u}}} \Bigg|_{t=T} \stackrel{(\text{Eqn. 47})}{=} \frac{\boldsymbol{\tau}^r}{\boldsymbol{\tau}^m} \circ \boldsymbol{\varphi}'(\mathcal{D}_{\boldsymbol{\tau}^r}^+ \{\mathbf{u}(T)\}) \circ (\mathbf{r}^{\text{trg}}(T) - \boldsymbol{\varphi}(\mathcal{D}_{\boldsymbol{\tau}^r}^+ \{\mathbf{u}(T)\})) \quad (53)$$

and obtain an initial condition for the adjoint system. Similarly, one can account for the initial conditions $g(\mathbf{u}, \dot{\mathbf{u}}, \mathbf{W})|_{t=0}$ of the dynamical system at $t = 0$ by adding another term to the Lagrangian, namely $\boldsymbol{\mu}^T g(\mathbf{u}(0), \dot{\mathbf{u}}(0), \mathbf{W})$. Both $\boldsymbol{\lambda}$ and $\boldsymbol{\mu}$ are vectors of Lagrangian multipliers that can be freely chosen because the constraints $\mathbf{h} = 0$ and $\mathbf{g} = 0$ are always satisfied by construction. Inspecting Eqn. 52, we observe that we can avoid calculating the term $\frac{d\mathbf{u}}{d\mathbf{W}}$ if the terms in square brackets are zero for all times t , which defines the dynamics of the adjoint system:

$$\frac{\partial C}{\partial \mathbf{u}} - \frac{d}{dt} \frac{\partial C}{\partial \dot{\mathbf{u}}} + \boldsymbol{\lambda}^T \frac{\partial \mathbf{h}}{\partial \mathbf{u}} - \dot{\boldsymbol{\lambda}}^T \frac{\partial \mathbf{h}}{\partial \dot{\mathbf{u}}} - \boldsymbol{\lambda}^T \frac{d}{dt} \frac{\partial \mathbf{h}}{\partial \dot{\mathbf{u}}} = \mathbf{0}. \quad (54)$$

Substituting the dynamic constraint \mathbf{h} defined in Eq. (47) yields the corresponding adjoint dynamics

$$\boldsymbol{\tau}^m \frac{d}{dt} \boldsymbol{\lambda}(t) = \boldsymbol{\lambda} - \left(\mathbf{1} - \boldsymbol{\tau}^r \frac{d}{dt} \right) [\boldsymbol{\varphi}' \circ (\mathbf{r}^{\text{trg}} - \mathbf{r})]. \quad (55)$$

This equation can be solved in a similar fashion to the forward dynamics (Eqn. 47). First, we conveniently define the adjoint operators

$$\mathcal{I}_\tau^+ \{ \mathbf{x}(t) \} = \frac{1}{\tau} \int_t^\infty ds \mathbf{x}(s) e^{-\frac{t-s}{\tau}} \quad (\text{discounted future}) \quad (56)$$

$$\mathcal{D}_\tau^- \{ \mathbf{x}(t) \} = \left(\mathbf{1} - \tau \frac{d}{dt} \right) \mathbf{x}(t). \quad (\text{lookback}). \quad (57)$$

Using these operators, we can write the dynamics of the adjoint variable $\boldsymbol{\lambda}$ as

$$\boldsymbol{\lambda}(t) = \mathcal{I}_{\tau_m}^+ \{ \mathcal{D}_{\tau_r}^- \{ \boldsymbol{\varphi}' \circ (\mathbf{r}^{\text{trg}} - \mathbf{r}) \} \}. \quad (58)$$

together with a boundary condition at $t = T$ given by Eqn. 53. Note that $\mathcal{I}_{\tau_m}^+$ integrates the dynamics into the future; this is the crucial reason why an AM weight update cannot be calculated online. Instead, we present a sample for the period T , and only afterwards integrate the adjoint dynamics *backwards in time* to obtain the Lagrange multiplier $\boldsymbol{\lambda}$ at all times $t \in [0, T]$. Finally, this allows us to calculate the gradient of the cost with respect to the synaptic weights

$$\nabla_{\mathbf{W}} \mathcal{L} = \left(\frac{d\mathcal{L}}{d\mathbf{W}} \right)^T = \int_0^T dt \boldsymbol{\lambda}(t) \mathbf{r}_{\text{in}}^T(t). \quad (59)$$

9.2 Hidden neurons

We now extend the proof to hidden layers. In order to do so, we introduce labels for all layers: \mathbf{u}_ℓ denotes the somatic voltage of a given layer ℓ . Lookahead $\mathcal{D}_{\tau_\ell}^+$ and low-pass filters $\mathcal{I}_{\tau_\ell}^-$ operate with layer-specific time constants τ_ℓ^r and τ_ℓ^m , respectively. The Lagrange multipliers $\boldsymbol{\lambda}_\ell$ are required to enforce the dynamics

$$\mathbf{h}_\ell(\mathbf{u}_\ell, \dot{\mathbf{u}}_\ell, \boldsymbol{\theta}, t) = \tau_\ell^m \dot{\mathbf{u}}_\ell + \mathbf{u}_\ell - \mathbf{W}_\ell \boldsymbol{\varphi} \left(\mathcal{D}_{\tau_{\ell-1}}^+ \{ \mathbf{u}_{\ell-1} \} \right) - \mathbf{b}_\ell = \mathbf{0}. \quad (60)$$

Remembering the layer-wise energy (cf. Eqn. 3)

$$E_\ell = \frac{1}{2} \|\mathbf{e}_\ell\|^2 = \frac{1}{2} \|\mathbf{u}_\ell + \tau_\ell^r \dot{\mathbf{u}}_\ell - \mathbf{W}_\ell \boldsymbol{\varphi}(\mathbf{u}_{\ell-1} + \tau_{\ell-1}^r \dot{\mathbf{u}}_{\ell-1}) - \mathbf{b}_\ell\|^2,$$

the goal of gradient descent in a hidden layer ℓ is to minimize the energy $E_{\ell+1}$ of the layer above, analogously to the cost \mathcal{C} in the output layer. As before, we introduce Lagrange multipliers $\boldsymbol{\lambda}_\ell$, and calculate

$$\frac{d\mathcal{L}}{d\mathbf{W}_\ell} = \frac{d}{d\mathbf{W}_\ell} \int_0^T dt \left[E_{\ell+1} + \boldsymbol{\lambda}_\ell^T \mathbf{h}_\ell \right].$$

Following the same reasoning as for the output layer, Lagrange multipliers $\boldsymbol{\lambda}_\ell$ are determined by (ref. Eq. (54))

$$\frac{\partial E_{\ell+1}}{\partial \mathbf{u}_\ell} - \frac{d}{dt} \frac{\partial E_{\ell+1}}{\partial \dot{\mathbf{u}}_\ell} + \boldsymbol{\lambda}_\ell^T \frac{\partial \mathbf{h}_\ell}{\partial \mathbf{u}_\ell} - \dot{\boldsymbol{\lambda}}_\ell^T \frac{\partial \mathbf{h}_\ell}{\partial \dot{\mathbf{u}}_\ell} - \boldsymbol{\lambda}_\ell^T \frac{d}{dt} \underbrace{\frac{\partial \mathbf{h}_\ell}{\partial \dot{\mathbf{u}}_\ell}}_{=\tau_\ell^m} = \mathbf{0}. \quad (61)$$

Working out the derivatives and assuming fixed time constants τ_ℓ^m , we find the adjoint dynamics of the hidden layer ℓ to be

$$- \left(\mathbf{1} - \tau_\ell^r \frac{d}{dt} \right) \left[\boldsymbol{\varphi}'_\ell \circ \mathbf{e}_{\ell+1}^T \mathbf{W}_{\ell+1} \right] + \boldsymbol{\lambda}_\ell^T - \tau_\ell^m \dot{\boldsymbol{\lambda}}_\ell^T = \mathbf{0}, \quad (62)$$

which after transposition can be written as

$$\tau_\ell^m \dot{\boldsymbol{\lambda}}_\ell = \boldsymbol{\lambda}_\ell - \mathcal{D}_{\tau_\ell}^- \left[\boldsymbol{\varphi}'_\ell \circ \mathbf{W}_{\ell+1}^T \mathbf{e}_{\ell+1} \right], \quad (63)$$

and is solved by

$$\boldsymbol{\lambda}_\ell = \mathcal{I}_{\tau_\ell^m}^+ \mathcal{D}_{\tau_\ell}^- \left[\boldsymbol{\varphi}'_\ell \circ \mathbf{W}_{\ell+1}^T \mathbf{e}_{\ell+1} \right]. \quad (64)$$

Considering Eqn. 58 and Eqn. 64, it now follows by induction that

$$\boldsymbol{\lambda}_\ell = \mathcal{I}_{\tau_\ell^m}^+ \mathcal{D}_{\tau_\ell}^- \left[\boldsymbol{\varphi}'_\ell \circ \mathbf{W}_{\ell+1}^T \boldsymbol{\lambda}_{\ell+1} \right]. \quad (65)$$

10 Simulation details

10.1 Small GLE nets

The main goal of Section 3.2 is to compare the dynamics and frequency response of the adjoint variables given by AM with the errors of GLE networks. In contrast to Section 3.1, where the BPTT baselines are obtained by backpropagating through the discretized forward dynamics of the GLE network, here we discretize the adjoint equations and integrate them numerically. The pseudocode comprising the forward and adjoint dynamics, together with synaptic plasticity, is given in Algorithm 2.

Algorithm 2 Simulation of the Adjoint Method baselines in Section 3.2

```

initialize network parameters  $\theta = \{W_{ij}, b_i, \tau_i^m, \tau_i^r\}$ 
initialize network states at  $t = 0$ :  $u_i(0), r_i(0)$ 
initialize adjoint variable  $\lambda$  states at  $t = T$ :  $\lambda_i(T)$ 
for time step  $t \in [0, T]$  with step size  $dt$  do
  for layer  $\ell$  from 1 to  $L$  do
    sum input currents:
       $\mathbf{I}_\ell(t) = \mathbf{W}_\ell(t)\mathbf{r}_{\ell-1}(t) + \mathbf{b}_\ell(t)$ 
    integrate input currents into membrane:
       $\Delta\mathbf{u}_\ell(t) \leftarrow (\boldsymbol{\tau}_\ell^m)^{-1} \circ (-\mathbf{u}_\ell(t) + \mathbf{I}_\ell(t))$ 
    update membrane voltages:
       $\mathbf{u}_\ell(t + dt) \leftarrow \mathbf{u}_\ell(t) + dt\Delta\mathbf{u}_\ell(t)$ 
    calculate prospective outputs:
       $\mathbf{r}_\ell(t + dt) \leftarrow \varphi(\mathbf{u}_\ell(t) + \boldsymbol{\tau}_\ell^r \circ \Delta\mathbf{u}_\ell(t))$ 
    store variables and update time index:
       $t \leftarrow t + dt$ 
  end for
end for
for layer  $\ell$  from  $L$  to 1 do
  for time step  $t \in [T, dt]$  with step size  $dt$  do
    calculate lookback  $\mathcal{D}_{\boldsymbol{\tau}_\ell^r}^-$ :
    if  $\ell = L$  then
       $\mathcal{D}_{\boldsymbol{\tau}_L^r}^- \leftarrow \left(1 - \frac{\boldsymbol{\tau}_L^r}{dt}\right) \circ \varphi'_L(t) \circ (\mathbf{r}^{\text{trg}}(t) - \mathbf{r}_L(t)) - \frac{\boldsymbol{\tau}_L^r}{dt} \circ \varphi'_L(t - dt) \circ (\mathbf{r}^{\text{trg}}(t - dt) - \mathbf{r}_L(t - dt))$ 
    else
       $\mathcal{D}_{\boldsymbol{\tau}_\ell^r}^- \leftarrow \left(1 - \frac{\boldsymbol{\tau}_\ell^r}{dt}\right) \circ \varphi'_\ell(t) \circ (\mathbf{W}_{\ell+1}^T \boldsymbol{\lambda}_{\ell+1}(t)) - \frac{\boldsymbol{\tau}_\ell^r}{dt} \circ \varphi'_\ell(t - dt) \circ (\mathbf{W}_{\ell+1}^T \boldsymbol{\lambda}_{\ell+1}(t - dt))$ 
    end if
    calculate adjoint variable:
       $\boldsymbol{\lambda}_\ell(t - dt) \leftarrow \boldsymbol{\lambda}_\ell(t) \circ e^{-dt/\boldsymbol{\tau}_\ell^m} + \mathcal{D}_{\boldsymbol{\tau}_\ell^r}^- \circ dt/\boldsymbol{\tau}_\ell^m$ 
    update time index:
       $t \leftarrow t - dt$ 
  end for
end for
Update synaptic weights:
 $\mathbf{W}_\ell \leftarrow \mathbf{W}_\ell - \eta_W \sum_{t=dt}^T \boldsymbol{\lambda}_\ell(t)\mathbf{r}_{\ell-1}^T(t)$ 

```

10.1.1 MNIST-1D reference baselines

All baselines were trained offline with BP(TT) (using PyTorch `autograd`) on the classification loss $\mathcal{L}_C = \sum_t \text{CE}(\hat{y}_t, y_t)\text{CE}(\hat{y}_t, y)$, with the one-hot target \hat{y} and the prediction $y = \text{Softmax}(\sum_{t=0}^T y_t)$, where T is the length of a sample. In contrast, GLE only uses the instantaneous cost $C = \text{CE}(\hat{y}, y)$. For the TCN and MLP baselines this corresponds to classical, spatial BP as they map time to (input) space and see the whole sequence at once. Note that the GRU implementation maintains a record of all hidden states for each sample and subsequently trains a readout layer on top of them. Therefore, despite the sequential processing, the GRU can only produce a prediction after the full sequence has been processed.

In particular, we use the following supersampling and model architectures:

- MLP: MNIST-1D sequences supersampled to 360 steps are fed into two consecutive hidden layers with 100 neurons each and ReLU activations in between, followed by a readout with 10 output neurons. The learning rate is 0.005.
- TCN: MNIST-1D sequences supersampled to 360 steps are fed into three layers of dilated convolutions with 25 channels each, kernel sizes $[5, 3, 3]$, stride 2, a dilation of $360/40 = 9$ followed by a linear readout with 125 input channels and 10 output neurons. The learning rate is 0.01.
- GRU: MNIST-1D sequences supersampled to 72 steps are streamed into single input unit that feeds into a single, bidirectional recurrent layer with 6 neurons followed by a linear layer on top of the hidden activations at all time steps, resulting in a bidirectional readout with $2 * 6 * 72 = 864$ input and 10 output neurons. The learning rate is 0.01.

Model	GLE (42k)	GLE (15k)	MLP ₀	TCN ₀	GRU ₀	MLP	TCN	GRU
number of parameters	42040	14956	15210	5210	5134	47210	11960	8974
online learning	yes	yes	no	no	no	no	no	no
streamed input	yes	yes	no	no	yes	no	no	yes
mean valid acc (last) / %	93.5 ± 0.9	91.7 ± 0.8	65.0 ± 1.2	93.7 ± 1.0	90.3 ± 2.5	65.5 ± 1.0	96.7 ± 0.9	94.0 ± 1.1

Table 2: Summary of the evaluated network models and their performance on the MNIST-1D dataset.

10.1.2 GSC reference baselines

As in the MNIST-1D dataset, both MLP and TCN networks were trained with spatial BP on a spatial representation of the temporal signal. The GRU network was trained offline with BPTT.

Model	GLE	MLP L	TCN L	GRU L	LSTM L
train samples	36923	36923	3	36923	36923
validation samples	4445	4445	4445	4445	4445
test samples	4890	4890	4890	4890	4890
MFS/MFCC	MFS	MFCC	MFCC	MFCC	MFCC
bins/coeffs	32	40	10	40	40
Fourier Window length	64 ms	40 ms	40 ms	40ms	20 ms
Fourier Window Stride	25 ms	40 ms	20 ms	20ms	20 ms
Batch size	256	100	100	100	100
Epochs	320	320	320	320	320
# params	1160262	495744	476734	498012	492620
acc / %	91.44 ± 0.23	88.00 ± 0.25	92.32 ± 0.28	94.93 ± 0.25	94.00 ± 0.19

Table 3: Summary of the evaluated network models and their performance on the GSC dataset. Additional details on the baseline model hyperparameters can be found in Appendix A of [1].

References

1. Zhang, Y., Suda, N., Lai, L. & Chandra, V. Hello Edge: Keyword Spotting on Microcontrollers. arXiv: 1711.07128 [cs.SD] (2018).